J. Fluid Mech. (2021), *vol*. 919, A26, doi:10.1017/jfm.2021.381

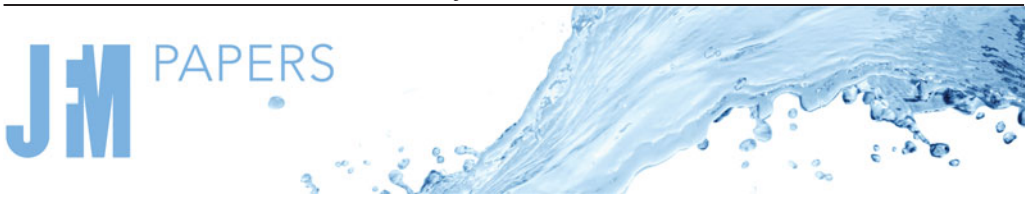

Transfer of internal energy fluctuation in compressible isotropic turbulence with vibrational non-equilibrium

Qinmin Zheng[1,2], Jianchun Wang[1,†], Md. Mahbub Alam[3], Bernd R. Noack[3,4], Hui Li[2] and Shiyi Chen[1,5]

[1]Guangdong Provincial Key Laboratory of Fundamental Turbulence Research and Applications, Center for Complex Flows and Soft Matter Research, Department of Mechanics and Aerospace Engineering, Southern University of Science and Technology, Shenzhen 518055, PR China

[2]School of Power and Mechanical Engineering, Wuhan University, Wuhan 430072, PR China

[3]Center for Turbulence Control, Harbin Institute of Technology, Shenzhen 518055, PR China

[4]Institut für Strömungsmechanik und Technische Akustik, Technische Universität Berlin, Müller-Breslau-Straße 8, D-10623 Berlin, Germany

[5]State Key Laboratory of Turbulence and Complex Systems, Peking University, Beijing 100871, PR China

(Received 30 September 2020; revised 17 April 2021; accepted 26 April 2021)

The transfer of internal energy fluctuation is numerically investigated for the stationary compressible isotropic turbulence in vibrational non-equilibrium with large-scale thermal forcing. We observe the spectra of velocity, solenoidal pressure component, density and temperatures all exhibiting the $k^{-5/3}$ scaling in the inertial range. The Helmholtz decomposition results reveal that the solenoidal velocity component predominates over the dilatational component. Fluctuations of the solenoidal velocity and pressure components are nearly insensitive to the turbulent Mach number and vibrational relaxation, while those of the dilatational velocity and pressure components are closely related to them. In addition, the weak and strong acoustic equilibrium hypotheses are verified. On global average, the dissipation of translational–rotational energy fluctuation stems mainly from the thermal conduction and vibrational relaxation, while effects of the dilatation and viscosity are negligible. For the vibrational energy fluctuation, the dilatation effect is insignificant, while the dissipation due to the thermal conduction is roughly equivalent to the production owing to the vibrational relaxation. The cascades of translational–rotational and vibrational energy fluctuations are mainly dominated by the solenoidal component of filtered velocity. The direct subgrid-scale (SGS) fluxes of translational–rotational and vibrational energy fluctuations due to the dilatational component of filtered velocity in the compression region are balanced by the reverse SGS fluxes in the expansion region. On the other hand, the dependencies of the SGS fluxes due to the solenoidal component of

† Email address for correspondence: wangjc@sustech.edu.cn

filtered velocity on the local compressibility are closely related to the relaxation effect. The sensibility gradually disappears as the relaxation effect weakens.

Key words: compressible turbulence, homogeneous turbulence

1. Introduction

The high-temperature compressible turbulence has been attracting interest from the fluid dynamics community due to its fascinating physical phenomena and frequent encounters in engineering applications (Anderson 2006; Bose 2014; Urzay 2018; Candler 2019; Colonna, Bonelli & Pascazio 2019). The elevated temperature in compressible turbulence may result in many processes, such as vibrational and electronic energies excitation, dissociation and ionization. Consequently, the high-temperature compressible turbulence may have several modes of internal energy (including translational, rotational, vibrational and electronic modes), and presents different gas properties when compared with the compressible turbulence at room temperature (Josyula 2015). Any redistribution of internal energy among different modes requires a number of molecular collisions and, hence, a certain characteristic time (relaxation time), which relies closely on the conditions of temperature and pressure. When the relaxation time is of the same order as the time scale of fluid flow, the thermal non-equilibrium effects must be taken into account. Generally, the relaxation time varies for different modes of internal energy. The translational and rotational modes may only need order 10–100 collisions, while the vibrational mode requires more than three orders of magnitude collisions to equilibrate (Hirschfelder *et al.* 1964; Rich & Treanor 1970). It suggests that the vibrational mode relaxes to equilibrium much slower than the translational and rotational modes. As a result, in many situations, the translational and rotational modes can be assumed to be in thermal equilibrium, while the vibrational mode is in thermal non-equilibrium (i.e. two-temperature model). The two-temperature model is widely adopted to study the thermal non-equilibrium issues, where the translational and rotational modes are characterized by the translational–rotational temperature (T_{tr}) and the vibrational mode by the vibrational temperature (T_v). The vibrational non-equilibrium thus indicates a delay between T_{tr} and T_v.

The vibrational non-equilibrium can have profound impacts on the flow dynamics. There are several studies that highlight the strong interaction between flow and vibrational non-equilibirum (Bertolotti 1998; Nompelis, Candler & Holden 2003; Shi *et al.* 2017; Fiévet & Raman 2018). In Knisely & Zhong (2020), for example, the impact of thermal non-equilibirium on the second and supersonic modes on a Mach 5 cold-wall cone was examined using direct numerical simulation. The thermochemical non-equilibrium and frozen thermochemical models were adopted. It was found that the flow was in both chemical non-equilibrium and thermal non-equilibrium in the nose region of the cone. However, the chemical non-equilibrium effects weakened significantly downstream of the nose, such that the flow was only considered to be in vibrational non-equilibrium. They also mentioned that at high-hypersonic conditions, predicting the heat flux to the vehicle was a critical design concern. Assuming a frozen thermochemical model and a thermal equilibrium model could respectively result in the transition occurring earlier and later than expected. In a worst-case scenario, the turbulent heat flux in an unexpected location could cause the vehicle to fail.

Nevertheless, the impact of turbulent fluctuation was ignored in most of the prior literature about vibrational non-equilibrium. Only a small percentage of investigations discussed the interaction between turbulent fluctuation and vibrational relaxation, as pioneered by Donzis & Maqui (2016), Khurshid & Donzis (2019) and Zheng *et al.* (2020) in compressible isotropic turbulence. As effects of the initial and boundary conditions are excluded, the compressible isotropic turbulence is an excellent flow model for studying the quantitative statistical properties of turbulence. This flow model is thus widely employed (Samtaney, Pullin & Kosović 2001; Liao, Peng & Luo 2010; Aluie, Li & Li 2012; Li, Zhang & He 2013; Ni 2015; Pan & Johnsen 2017; Sciacovelli, Cinnella & Grasso 2017). Donzis & Maqui (2016) investigated the stationary compressible isotropic turbulence in vibrational equilibrium and non-equilibrium. They found that significant energy transfers between the translational–rotational and vibrational modes arose due to the departure from equilibrium and finite-time vibrational relaxation. The strong departures from thermal equilibrium were observed at small scales, and the spectral behaviour of vibrational energy was described by the classical phenomenology for passive scalars. Later, Khurshid & Donzis (2019) studied the interaction of decaying compressible turbulence with vibrational non-equilibrium at low turbulent Mach numbers. It was revealed that a larger initial vibrational energy resulted in a faster effective decay of vibrational non-equilibrium. The relaxation towards equilibrium leads to increases of the translational–rotational temperature and viscosity. The dissipation thus increases temporarily and further results in a faster turbulence decay. Zheng *et al.* (2020) discussed the effects of compressibility and vibrational relaxation on the statistical properties of vibrational rate and dissipation/production of vibrational energy fluctuation, in the stationary compressible isotropic turbulence with vibrational non-equilibrium. When the relaxation time is small enough, on average, the internal energy transfers from the translational–rotational to vibrational modes in the compression region and in the inverse direction in the expansion region. The strength of internal energy exchange is enhanced by the flow compressibility, and weakens as the relaxation time increases. The dissipation/production of vibrational energy fluctuation results from the effects of dilatation, thermal conduction and vibrational relaxation, and the effects are quit different between the weakly and highly compressible turbulence.

There have been a number of investigations on the kinetic energy transfer in compressible isotropic turbulence (Aluie 2011, 2013; Eyink & Drivas 2018; Wang *et al.* 2018; Schmidt & Grete 2019). It extends the traditional Richardson–Kolmogorov–Onsager picture of kinetic energy cascade (Kolmogorov 1991; Frisch 1995; Cardy, Falkovich & Gawedzki 2008; Sagaut & Cambon 2008; Alexakis & Biferale 2018) to the compressible turbulence. However, the transfers of thermodynamic variables (such as temperature, entropy, internal energy, etc.) are rarely investigated. Wang *et al.* (2019) numerically investigated the cascades of temperature and entropy fluctuations in the stationary compressible isotropic turbulence with the large-scale thermal forcing. The introduction of large-scale thermal forcing was found to have significant impacts on the properties of compressible turbulence, such as the flow compressibility and the transfers of temperature and entropy. It was revealed that both temperature and entropy fluctuations cascaded from large- to small-scale motions, and the effect of compressibility on the cascade of temperature fluctuation was much stronger than that of entropy fluctuation.

The advent of vibrational non-equilibrium renders the energy exchange in compressible turbulence more complicated. The energy exchanges between translational–rotational and vibrational modes via vibrational relaxation. However, there is no direct exchange path between the vibrational and kinetic energies. In present simulations, different from the

previous works (Donzis & Maqui 2016; Khurshid & Donzis 2019; Zheng *et al.* 2020), both large-scale momentum forcing and thermal forcing are adopted, to maintain the turbulence in a statistically stationary state and to inject the large-scale temperature fluctuation. We will mainly focus on the combined impact of vibrational relaxation and large-scale thermal forcing on the statistical properties of turbulence and the transfer of internal energy fluctuation.

The rest of paper is organized as follows. In § 2 we recapitulate the governing equations, thermodynamic and transport properties of compressible turbulence, and give a brief description of numerical methodology. The one-point statistics of present simulated flows are given in § 3. We introduce the instantaneous isosurfaces, contours and probability density functions of normalized dilatation, and the spectra of velocity, pressure, density and temperatures in § 4. The strong acoustic equilibrium hypothesis is also verified in this section. The effects of vibrational relaxation and flow compressibility on the dissipation, production and transfer of the internal energy fluctuation are presented in §§ 5 and 6. Finally, concluding remarks are provided in § 7.

2. Governing equations and numerical method

In present simulations we consider the non-reactive mono-species gases and Newtonian fluids for which the dynamic viscosity depends only on temperature. The governing equations for compressible turbulence in vibrational non-equilibrium can be written in the dimensionless form as

$$\frac{\partial \rho}{\partial t} + \frac{\partial (\rho u_j)}{\partial x_j} = 0, \tag{2.1}$$

$$\frac{\partial (\rho u_i)}{\partial t} + \frac{\partial [\rho u_i u_j + p\delta_{ij}]}{\partial x_j} = \frac{1}{Re}\frac{\partial \sigma_{ij}}{\partial x_j} + \mathcal{F}_i, \tag{2.2}$$

$$\frac{\partial \varepsilon}{\partial t} + \frac{\partial [(\varepsilon + p)u_j]}{\partial x_j} = \frac{1}{\alpha}\frac{\partial}{\partial x_j}\left(\kappa_{tr}\frac{\partial T_{tr}}{\partial x_j} + \kappa_v \frac{\partial T_v}{\partial x_j}\right) + \frac{1}{Re}\frac{\partial (\sigma_{ij}u_i)}{\partial x_j} - \Lambda + \mathcal{F}_I + \mathcal{F}_j u_j, \tag{2.3}$$

$$\frac{\partial E_v}{\partial t} + \frac{\partial (E_v u_j)}{\partial x_j} = \frac{1}{\alpha}\frac{\partial}{\partial x_j}\left(\kappa_v \frac{\partial T_v}{\partial x_j}\right) + \frac{E_v^* - E_v}{\tau_v}, \tag{2.4}$$

$$p = \rho T_{tr}/(\gamma_r M^2), \tag{2.5}$$

where the dimensionless density, velocity components, pressure, translational–rotational and vibrational temperatures are respectively denoted as ρ, u_i, p, T_{tr} and T_v. The $\mathcal{F}_i$ and $\mathcal{F}_I$ are the large-scale forcings to the fluid momentum and translational–rotational energy, respectively. The velocity field is decomposed into a solenoidal component and a dilatational component. The large-scale forcing to the solenoidal velocity component is employed to maintain the velocity fluctuation within the two lowest wavenumber shells at prescribed levels, while the dilatational velocity component is left untouched. The large-scale forcing to the translational–rotational temperature is similar, while the prescribed levels are one percent of that for the solenoidal velocity component. The detailed forcing strategy has been given in Appendix A. Furthermore, the uniform thermal cooling function Λ is adopted to sustain the internal energy in a statistically steady state (Passot, Vázquez-Semadeni & Pouquet 1995; Wang *et al.* 2010). The T_{tr} is employed in the equation of state (2.5), because the pressure mainly stems from the translational motion of molecules (Vincenti & Kruger 1965). The reference Reynolds number $Re \equiv \rho_r U_r L_r/\mu_r$,

the reference Mach number $M \equiv U_r/c_r$ and the reference Prandtl number $Pr \equiv \mu_r C_{p_r}/\kappa_r$ are three governing parameters. Here, ρ_r, U_r, L_r and μ_r are the reference density, velocity, length and viscosity coefficients, respectively. The reference speed of sound is given by $c_r = \sqrt{\gamma_r R T_r}$, where R is the specific gas constant and $T_r = 1200K$ is the reference temperature. The $\gamma_r \equiv C_{p_r}/C_{v_r}$ is the ratio of specific heat at constant pressure C_{p_r} to that at constant volume C_{v_r}. The γ_r approximately equals 1.324 based on the specific heat ratio of dry air at $T_r = 1200$ K (Vincenti & Kruger 1965; Anderson 2006). The dimensionless parameter α is given as $\alpha \equiv PrRe(\gamma_r - 1)M^2$, where Pr is set to be 0.71.

The total energy per unit volume (ε), the vibrational energy per unit volume in thermal equilibrium (E_v^*) and non-equilibrium (E_v), and the viscosity stress (σ_{ij}) are respectively given as

$$\varepsilon = \rho\left(e_{tr} + e_v + \frac{1}{2}u_j u_j\right) = \frac{5}{2}p + E_v + \frac{1}{2}\rho(u_j u_j), \tag{2.6}$$

$$E_v^* = \rho e_v^* = \frac{\rho\theta_v}{\gamma_r M^2[\exp(\theta_v/T_{tr}) - 1]}, \tag{2.7}$$

$$E_v = \rho e_v = \frac{\rho\theta_v}{\gamma_r M^2[\exp(\theta_v/T_v) - 1]}, \tag{2.8}$$

$$\sigma_{ij} = \mu\left(\frac{\partial u_i}{\partial x_j} + \frac{\partial u_j}{\partial x_i}\right) - \frac{2}{3}\mu\theta\delta_{ij}, \tag{2.9}$$

where e_{tr} is the translational–rotational energy per unit mass, while e_v^* and e_v are the vibrational energy per unit mass in thermal equilibrium and non-equilibrium, respectively. The θ_v is the characteristic vibrational temperature normalized by T_r, while $\theta = \partial u_k/\partial x_k$ is the velocity divergence. The temperature-dependent viscosity (μ) and thermal conductivity coefficients (κ_{tr} and κ_v) are specified by Sutherland's and Eucken's laws. For their detailed expressions, please refer to our previous publication (Zheng *et al.* 2020).

In vibrational energy governing equation (2.4), the widely used Landau–Teller relaxation model is adopted for the vibrational rate $Q_v = (E_v^* - E_v)/\tau_v$. The dimensionless local relaxation time (τ_v) depends closely on the local temperature and pressure, and is calculated roughly by (Vincenti & Kruger 1965)

$$\tau_v = (C/p)\exp(K_2/T_{tr})^{1/3}, \tag{2.10}$$

where C and K_2 are the dimensionless constants relating to the molecular structure of gases. Following the previous literature (Donzis & Maqui 2016; Khurshid & Donzis 2019; Zheng *et al.* 2020), the dimensionless parameter $\langle K_\tau\rangle = \langle\tau_v\rangle/\tau_\eta$ is adopted to characterize the time scale of the relaxation process. The $\langle\cdot\rangle$ operator stands for spatial average. The $\tau_\eta = [\langle\mu/(Re\rho)\rangle/\epsilon]^{1/2}$ is the Kolmogorov time scale, $\epsilon = \langle\sigma_{ij}S_{ij}/Re\rangle/\langle\rho\rangle$ is the kinetic energy dissipation rate per unit mass due to viscosity and $S_{ij} = (\partial u_i/\partial x_j + \partial u_j/\partial x_i)/2$ is the strain rate tensor. The K_2 is set to be 2000.0, close to that in real gases. For instance, K_2 is respectively about 2460 and 1590 for oxygen and nitrogen molecules (Vincenti & Kruger 1965). Moreover, the constant C is adjusted to obtain a specific $\langle K_\tau\rangle$ value.

The governing equations of compressible turbulence are solved in conservative form in a cubic box with the side length equaling 2π and a 512^3 grid resolution. The periodic boundary conditions in all three spatial directions are employed. The hybrid compact-weighted essentially non-oscillatory (compact-WENO) scheme is applied in present simulations. The hybrid scheme combines the eighth-order central compact finite difference scheme in smooth regions and the seventh-order WENO scheme in

Case	Re	Pr	M	θ_v	$\langle K_\tau \rangle$	Re_λ	M_t	$\eta/\Delta x$	L_f/η	T_e/τ_η	ϵ	$\mathcal{H}$	θ'
I_1	400	0.71	0.099	1.0	0.16	155.53	0.22	1.04	114.40	18.11	0.72	3.39	0.91
I_2	400	0.71	0.099	1.0	0.77	158.40	0.22	1.04	114.24	18.04	0.70	1.70	0.58
I_3	400	0.71	0.099	1.0	4.00	155.90	0.22	1.04	114.78	18.19	0.71	1.36	0.56
I_4	400	0.71	0.099	1.0	9.80	160.24	0.22	1.05	113.23	17.67	0.67	1.24	1.53

Table 1. Simulation parameters and resulting flow statistics for the weakly compressible turbulence. Considering $\langle K_\tau \rangle$ effects. Here $M_t \approx 0.22$.

Case	Re	Pr	M	θ_v	$\langle K_\tau \rangle$	Re_λ	M_t	$\eta/\Delta x$	L_f/η	T_e/τ_η	ϵ	$\mathcal{H}$	θ'
I_2	400	0.71	0.099	1.0	0.77	158.40	0.22	1.04	114.24	18.04	0.70	1.70	0.58
I_5	400	0.71	0.099	3.0	0.84	157.71	0.22	1.06	114.05	17.92	0.65	0.58	1.09
I_6	400	0.71	0.099	5.0	0.82	158.12	0.22	1.06	113.23	17.71	0.66	0.08	1.78

Table 2. Simulation parameters and resulting flow statistics for the weakly compressible turbulence. Considering θ_v effects. Here $M_t \approx 0.22$.

Case	Re	Pr	M	θ_v	$\langle K_\tau \rangle$	Re_λ	M_t	$\eta/\Delta x$	L_f/η	T_e/τ_η	ϵ	$\mathcal{H}$	θ'
II_1	400	0.71	0.296	1.0	0.19	153.36	0.68	1.01	114.34	18.26	0.80	1.07	2.50
II_2	400	0.71	0.296	1.0	0.86	159.63	0.68	1.04	113.30	17.78	0.70	0.69	2.10
II_3	400	0.71	0.296	1.0	4.27	160.64	0.66	1.06	112.46	17.65	0.66	0.32	1.67
II_4	400	0.71	0.296	1.0	7.98	160.31	0.67	1.05	114.05	17.81	0.66	0.22	2.09

Table 3. Simulation parameters and resulting flow statistics for the highly compressible turbulence. Considering $\langle K_\tau \rangle$ effects. Here $M_t \approx 0.68$.

shock regions. The time derivative is approximated by the standard Runge–Kutta method. For more details of the numerical method, please refer to Lele (1992), Gottlieb & Shu (1998), Balsara & Shu (2000) and Wang *et al.* (2010). After the system reaches the statistically stationary state, sixty-one flow fields, spanning the time period of $9.01 \lesssim t/T_e \lesssim 14.41$, are employed to obtain the statistical averages of interested quantities. Here, $T_e(=\sqrt{3}L_f/u')$ is the large eddy turnover time and L_f is the integral length scale.

3. One-point statistics of compressible turbulence

The overall statistics of present simulations are summarized in tables 1–4. The reference Reynolds number and Prandtl number are kept constant ($Re = 400$ and $Pr = 0.71$). The reference Mach number (M) is set to be 0.099 and 0.296. For each Mach number, we control the characteristic vibrational temperature (θ_v) and relaxation time (τ_v) to investigate the vibrational non-equilibrium effect. In present simulations, three different θ_v ($\theta_v = 1.0$, 3.0 and 5.0) are employed. A lower θ_v suggests an easier excitation of the vibrational mode. Meanwhile, the τ_v is normalized as $\langle K_\tau \rangle$. The $\langle K_\tau \rangle$ approximately equals 0.16–9.80 for the $M = 0.099$ cases, and 0.19–7.98 for the $M = 0.296$ cases. Here, cases I_1–I_4 and cases II_1–II_4 (tables 1 and 3) are used to discuss the effect of $\langle K_\tau \rangle$, while cases I_2, I_5, I_6 and cases II_2, II_5, II_6 (tables 2 and 4) are adopted to study the effect of θ_v.

The Taylor microscale Reynolds number (Re_λ) and turbulent Mach number (M_t) are respectively defined as

$$Re_\lambda = Re\frac{\langle\rho\rangle u'\lambda}{\sqrt{3}\langle\mu\rangle} \quad \text{and} \quad M_t = M\frac{u'}{\langle\sqrt{T_{tr}}\rangle}, \tag{3.1a,b}$$

Case	Re	Pr	M	θ_v	$\langle K_\tau \rangle$	Re_λ	M_t	$\eta/\Delta x$	L_f/η	T_e/τ_η	ϵ	$\mathcal{H}$	θ'
II_2	400	0.71	0.296	1.0	0.86	159.63	0.68	1.04	113.30	17.78	0.70	0.69	2.10
II_5	400	0.71	0.296	3.0	0.97	153.98	0.68	1.01	114.40	18.17	0.78	0.16	2.57
II_6	400	0.71	0.296	5.0	0.91	155.12	0.67	1.03	114.46	18.08	0.72	0.02	2.95

Table 4. Simulation parameters and resulting flow statistics for the highly compressible turbulence. Considering θ_v effects. Here $M_t \approx 0.68$.

where the root mean square (r.m.s.) value of velocity magnitude and the Taylor microscale are respectively given by

$$u' = \sqrt{\langle u_1^2 + u_2^2 + u_3^2 \rangle} \tag{3.2}$$

$$\text{and} \quad \lambda = \sqrt{\frac{\langle u_1^2 + u_2^2 + u_3^2 \rangle}{\langle (\partial u_1/\partial x_1)^2 + (\partial u_2/\partial x_2)^2 + (\partial u_3/\partial x_3)^2 \rangle}}. \tag{3.3}$$

Here, the M_t approximately equals 0.22 and 0.68 for $M = 0.099$ and 0.296 cases, respectively. The Re_λ is considered to be constant for all cases. The $Re_\lambda \approx 157.5$, with the largest deviation at 2.0 % (tables 1–4).

The resolution parameter $\eta/\Delta x$ is in the range of $1.01 \lesssim \eta/\Delta x \lesssim 1.06$, where Δx is the grid length in each direction (tables 1–4). The resolution parameter $k_{max}\eta$ is therefore in $3.17 \lesssim k_{max}\eta \lesssim 3.33$, where the largest wavenumber k_{max} is half of the number of grids N in each direction (i.e. $k_{max} = N/2$). According to the previous grid refinement studies (Wang *et al.* 2011), the grid resolutions $k_{max}\eta \geq 2.77$ are enough for the convergence of flow statistics, including energy spectra at different wavenumbers, probability density functions (PDFs) of normalized dilatation and vorticity, etc.

The integral length scale is calculated by

$$L_f = \frac{3\pi}{2(u')^2} \int_0^\infty \frac{E^u(k)}{k} \mathrm{d}k, \tag{3.4}$$

where $E^u(k)$ is the spectrum of kinetic energy per unit mass. The ratios L_f/η and T_e/τ_η respectively represent the spatial and time scales in the simulated flows. The $\eta = [\langle \mu/(Re\rho) \rangle^3/\epsilon]^{1/4}$ is the Kolmogorov length scale. Presently, $L_f/\eta \approx 113.8$ and $T_e/\tau_\eta \approx 17.9$ (tables 1–4). The kinetic energy dissipation rate due to viscosity (ϵ) is about 0.70 for both the $M_t \approx 0.22$ and 0.68 cases.

The vibrational rate represents the energy exchange rate between the translational–rotational and vibrational modes. Its r.m.s. value ($Q_{v,rms}$) can be employed to assess the strength of energy exchange. However, the proportion of vibrational mode in the internal energy should also be taken into account. The spatially averaged ratio of the vibrational energy to the total internal energy (i.e. $\langle E_v^*/[(5/2)p + E_v^*] \rangle$) approximately equals 18.88 %, 5.92 % and 1.34 % with $\theta_v = 1.0$, 3.0 and 5.0, respectively. Here, the parameter $\mathcal{H}(= \langle E_v^*/[(5/2)p + E_v^*] \rangle Q_{v,rms})$ is adopted, combining effects of θ_v and $\langle K_\tau \rangle$. For the $M_t \approx 0.22$ cases, $\mathcal{H}$ decreases from 3.39 to 1.24 as $\langle K_\tau \rangle$ increases from 0.16 to 9.80 (cases I_1–I_4, table 1), and decreases from 1.70 to 0.08 with θ_v varying from 1.0 to 5.0 (cases I_2, I_5 and I_6, table 2). For the $M_t \approx 0.68$ cases, $\mathcal{H}$ decreases from 1.07 to 0.22 as $\langle K_\tau \rangle$ increases from 0.19 to 7.98 (cases II_1–II_4, table 3), and decreases from 0.69 to 0.02 with θ_v varying from 1.0 to 5.0 (cases II_2, II_5 and II_6, table 4). It reveals that the increase of $\langle K_\tau \rangle$ and θ_v weakens the energy exchange among internal energy modes. In addition, $\mathcal{H}$

Case	u'	u^D_{rms}	u^S_{rms}	u^D_{rms}/u^S_{rms}	p_{rms}	p^D_{rms}	p^S_{rms}	p^D_{rms}/p^S_{rms}	χ	$\mathcal{D}$
I_1	2.28	0.53	2.22	0.24	5.23	5.12	1.41	3.62	1.04	1.10
I_2	2.28	0.40	2.24	0.18	4.00	3.82	1.47	2.59	1.06	0.83
I_3	2.28	0.39	2.24	0.18	4.10	3.91	1.40	2.80	1.01	0.80
I_4	2.28	0.58	2.20	0.26	6.00	5.92	1.47	4.02	0.97	1.22

Table 5. Statistics of weak acoustic equilibrium hypothesis and fluctuations of velocity and pressure components. Considering $\langle K_\tau \rangle$ effects. Here $M_t \approx 0.22$.

for the $M_t \approx 0.22$ cases is much larger than its counterpart for the $M_t \approx 0.68$ cases, which is attributed to the large-scale thermal forcing.

The velocity divergence is always used to measure the local rate of compression ($\theta < 0$) or expansion ($\theta > 0$). Its r.m.s. value (θ') represents the flow compressibility to some extent. As shown in tables 1–4, for the $M_t \approx 0.22$ cases, θ' (≈0.56–1.78) is smaller than that for the $M_t \approx 0.68$ cases ($\theta' \approx 1.67$–2.95). For the $M_t \approx 0.22$ cases (table 1), θ' decreases from 0.91 to 0.57 with $\langle K_\tau \rangle$ increasing from 0.16 to 0.77, keeps almost constant in the range of $0.77 \leq \langle K_\tau \rangle \leq 4.00$, and jumps to 1.53 with $\langle K_\tau \rangle \approx 9.80$. For the $M_t \approx 0.68$ cases (table 3), θ' decreases from 2.50 to 1.67 as $\langle K_\tau \rangle$ increases from 0.19 to 4.27, and jumps to 2.09 with $\langle K_\tau \rangle \approx 7.98$. It suggests that the flow compressibility relates closely to the relaxation time, particularly for the $M_t \approx 0.22$ cases. With θ_v varying from 1.0 to 5.0, θ' grows from 0.58 to 1.78 (cases I_2, I_5 and I_6, table 2) for the $M_t \approx 0.22$ cases, and from 2.10 to 2.95 (cases II_2, II_5 and II_6, table 4) for the $M_t \approx 0.68$ cases. That is, the increase of θ_v enhances the flow compressibility.

The Helmholtz decomposition is employed to decompose the velocity field $\boldsymbol{u}$ into a solenoidal component $\boldsymbol{u}^S$ and a dilatational component $\boldsymbol{u}^D$ as

$$\boldsymbol{u} = \boldsymbol{u}^S + \boldsymbol{u}^D, \tag{3.5}$$

where $\nabla \cdot \boldsymbol{u}^S = 0$ and $\nabla \times \boldsymbol{u}^D = 0$. Their r.m.s.values are respectively defined as $u^S_{rms} = \sqrt{\langle (u^S_1)^2 + (u^S_2)^2 + (u^S_3)^2 \rangle}$ and $u^D_{rms} = \sqrt{\langle (u^D_1)^2 + (u^D_2)^2 + (u^D_3)^2 \rangle}$. The r.m.s. values of velocity and its components for the $M_t \approx 0.22$ and 0.68 cases are presented in tables 5–8. Obviously, u^S_{rms} is close to u', while u^D_{rms} is significantly smaller than u'. It implies that the solenoidal velocity component is predominant over the dilatational velocity component. For the $M_t \approx 0.22$ cases, u^D_{rms}/u^S_{rms} dwindles from 0.24 for cases I_1 to 0.18 for cases I_2 and I_3, and jumps to 0.26 for cases I_4 (table 5). Moreover, u^D_{rms}/u^S_{rms} increases from 0.18 to 0.31 with θ_v varying from 1.0 to 5.0 (table 6). Obviously, the variation of u^D_{rms}/u^S_{rms} is consistent with that of θ'. As will be illustrated in § 4, the instantaneous isosurfaces and contours of θ/θ' for cases I_1–I_3 are significantly different from cases I_4–I_6. The vibrational relaxation has a great impact on the compression and expansion motions for the $M_t \approx 0.22$ cases. For the $M_t \approx 0.68$ cases (table 7), $u^D_{rms}/u^S_{rms} \approx 0.19$ with $\langle K_\tau \rangle \approx 0.19$ and 0.86 (cases II_1, II_2), and slightly decreases to 0.15 as $\langle K_\tau \rangle$ increases to 7.98 (cases II_4). Moreover, u^D_{rms}/u^S_{rms} keeps almost constant (≈0.20) with θ_v varying from 1.0 to 5.0 (cases II_2, II_5, II_6, table 8). It means that for the $M_t \approx 0.68$ cases, the increase of $\langle K_\tau \rangle$ weakens the fluctuation of dilatational velocity component, while θ_v does not affect significantly on it.

Similar to the velocity field decomposition, the pressure fluctuation can be decomposed into a solenoidal component p^S and a dilatational component p^D, i.e. $p' = p^S + p^D$. The solenoidal pressure component satisfies the incompressible pressure Poisson

Case	u'	u^D_{rms}	u^S_{rms}	u^D_{rms}/u^S_{rms}	p_{rms}	p^D_{rms}	p^S_{rms}	p^D_{rms}/p^S_{rms}	χ	$\mathcal{D}$
I_2	2.28	0.40	2.24	0.18	4.00	3.82	1.47	2.59	1.06	0.83
I_5	2.25	0.57	2.18	0.26	5.69	5.64	1.33	4.25	1.01	1.23
I_6	2.27	0.67	2.16	0.31	6.86	6.83	1.42	4.82	0.99	1.48

Table 6. Statistics of weak acoustic equilibrium hypothesis and fluctuations of velocity and pressure components. Considering θ_v effects. Here $M_t \approx 0.22$.

Case	u'	u^D_{rms}	u^S_{rms}	u^D_{rms}/u^S_{rms}	p_{rms}	p^D_{rms}	p^S_{rms}	p^D_{rms}/p^S_{rms}	χ	$\mathcal{D}$
II_1	2.33	0.42	2.29	0.18	1.73	1.33	1.28	1.04	1.06	0.27
II_2	2.30	0.44	2.25	0.20	1.86	1.41	1.43	0.98	1.06	0.30
II_3	2.27	0.37	2.24	0.16	1.58	1.18	1.24	0.95	1.04	0.25
II_4	2.26	0.34	2.24	0.15	1.69	1.08	1.42	0.76	1.07	0.23

Table 7. Statistics of weak acoustic equilibrium hypothesis and fluctuations of velocity and pressure components. Considering $\langle K_\tau \rangle$ effects. Here $M_t \approx 0.68$.

Case	u'	u^D_{rms}	u^S_{rms}	u^D_{rms}/u^S_{rms}	p_{rms}	p^D_{rms}	p^S_{rms}	p^D_{rms}/p^S_{rms}	χ	$\mathcal{D}$
II_2	2.30	0.44	2.25	0.20	1.86	1.41	1.43	0.98	1.06	0.30
II_5	2.32	0.46	2.28	0.20	1.86	1.46	1.38	1.06	1.05	0.30
II_6	2.29	0.44	2.24	0.20	1.88	1.44	1.40	1.03	1.03	0.30

Table 8. Statistics of weak acoustic equilibrium hypothesis and fluctuations of velocity and pressure components. Considering θ_v effects. Here $M_t \approx 0.68$.

equation as

$$\nabla^2 p^S = -\langle \rho \rangle \frac{\partial u_i^S}{\partial x_j} \frac{\partial u_j^S}{\partial x_i}. \tag{3.6}$$

The statistics of pressure and its solenoidal and dilatational components for the presently simulated flows are summarized in tables 5–8.

For the $M_t \approx 0.22$ cases, the pressure fluctuation ($p_{rms} \approx 4.00$–6.86) is much larger than its counterpart ($p_{rms} \approx 1.58$–1.88) for the $M_t \approx 0.68$ cases. It is attributed to the sharp increase of fluctuation of the dilatational pressure component (p^D_{rms}). As will be shown in § 4, the enhanced fluctuations are mainly located at low wavenumbers due to the large-scale thermal forcing.

For the $M_t \approx 0.22$ cases (tables 5 and 6), $p^D_{rms}/p^S_{rms} \approx 2.59$–$4.82$. That is, the dilatational component is predominant over the solenoidal component in pressure fluctuation. With $\langle K_\tau \rangle \approx 0.16$, case I_1 approaches the vibrational equilibrium state, for which the injected temperature fluctuation instantly transfers to the vibrational temperature, and the vibrational relaxation effect is relatively weaker. Consequently, the large-scale thermal forcing enhancing the flow compressibility is expected. As $\langle K_\tau \rangle$ increases, the vibrational relaxation effect gets stronger, and suppresses the flow compressibility. Furthermore, it might be speculated that if $\langle K_\tau \rangle$ is large enough, the exchange between the translational–rotational and vibrational energies would be extremely weakened (i.e. frozen thermal model, Vincenti & Kruger (1965)). In this situation, the translational–rotational and vibrational energies may be treated as two independent components, and the flow compressibility would be enhanced again by the large-scale thermal forcing. Consequently, as shown in table 5, p^D_{rms}/p^S_{rms} approximately equals 3.62

for case I_1, drops sharply to ≈2.70 for cases I_2 and I_3 as $\langle K_\tau \rangle$ increases from 0.16 to 4.00, and jumps to 4.02 for case I_4 with $\langle K_\tau \rangle \approx 9.80$. Moreover, with θ_v varying from 1.0 to 5.0, the vibrational relaxation effect is attenuated. The p^D_{rms}/p^S_{rms} thus increases monotonously from 2.59 to 4.82 (cases I_2, I_5 and I_6, table 6).

For the $M_t \approx 0.68$ cases (tables 7 and 8), $p^D_{rms}/p^S_{rms} \approx 0.76$–$1.06$. It suggests that in these cases, the dilatational component is comparable to the solenoidal component in pressure fluctuation. For the $M_t \approx 0.68$ cases, the fluctuation of translational–rotational temperature at large-scale motions may be comparable to the large-scale thermal forcing adopted in the presented simulations. This might be the reason why the effect of large-scale thermal forcing on the flow compressibility is inconspicuous for the $M_t \approx 0.68$ cases (tables 3 and 4). Consequently, the variance of p^D_{rms}/p^S_{rms} for the $M_t \approx 0.68$ cases is not as obvious as that for the $M_t \approx 0.22$ cases. As $\langle K_\tau \rangle$ increases from 0.86 to 7.98, p^D_{rms}/p^S_{rms} dwindles from 1.04 to 0.76. It is expected that when $\langle K_\tau \rangle$ is large enough, p^D_{rms}/p^S_{rms} would not increase, but approaches a constant. The p^D_{rms}/p^S_{rms} keeps approximately constant (≈1.03) with θ_v varying from 1.0 to 5.0.

Note that, if the dilatational velocity component is dominated by acoustic waves, there are equilibrium relations between the dilatational pressure and velocity components in weak and strong forms (Sagaut & Cambon 2008; Jagannathan & Donzis 2016). The weak and strong acoustic equilibrium hypotheses can be respectively expressed as

$$\chi = \langle p \rangle \gamma_r M_t (u^D_{rms}/u')/p^D_{rms} \approx 1.0 \tag{3.7}$$

$$\text{and} \quad E^{p^D}(k) = 2.0\gamma_r \langle \rho \rangle \langle p \rangle E^{u^D}(k). \tag{3.8}$$

For the weak form, the equilibrium hypothesis between dilatational components of pressure and velocity is expected to be valid in a global average sense. However, for the strong form, the equilibrium hypothesis between dilatational components of pressure and velocity is established for each wavenumber.

As mentioned in Jagannathan & Donzis (2016), for the stationary turbulence without large-scale thermal forcing, $p^D_{rms}/p^S_{rms} \approx 0.12$ and 0.22 with $M_t \approx 0.1$ and 0.2, while $p^D_{rms}/p^S_{rms} \approx 1.07$, 1.16 and 1.19 with $M_t \approx 0.3$, 0.4 and 0.6, respectively. The Re_λ is about 160. The χ approximately equals 0.65, 0.67, 1.06, 1.01 and 1.10 with $M_t \approx 0.1, 0.2, 0.3, 0.4$ and 0.6, respectively. Furthermore, for low M_t (≈0.1, 0.2) flows, the spectra content of p^D is smaller than that of u^D at all scales with a stronger departure at intermediate and high wavenumbers. Beyond the threshold $M_t \approx 0.3$, the spectra of p^D and u^D begin to overlap in an increasingly wider range of scales. That is, for the stationary turbulence without large-scale thermal forcing, the weak and strong forms of acoustic equilibrium hypotheses are valid only at high M_t (e.g. $M_t \geq 0.3$). For the stationary turbulence with large-scale thermal forcing, Wang *et al.* (2019) found $u^D_{rms}/u^S_{rms} \approx 0.37$ and 0.24 with $M_t \approx 0.20$ and 0.60, respectively, where Re_λ is about 252. That is, the large-scale thermal forcing enhances the flow compressibility of the low M_t turbulence. Moreover, they mentioned that the weak and strong forms of acoustic equilibrium hypotheses were valid for both the $M_t \approx 0.20$ and 0.60 cases.

The statistics of weak acoustic equilibrium hypothesis are given in tables 5–8. Interestingly, $\chi (= \langle p \rangle \gamma_r M_t (u^D_{rms}/u')/p^D_{rms})$ is close to 1.0 for both the $M_t \approx 0.22$ and 0.68 cases. It indicates that in a global average sense, the dilatational velocity component is dominated by acoustic waves in the presently simulated flows. The weak acoustic equilibrium hypothesis can be rewritten as

$$p^D_{rms}/\langle p \rangle = \gamma_r M_t u^D_{rms}/u'. \tag{3.9}$$

The above observations reveal that on spatial average, the fluctuation of the dilatational pressure component in present simulations can collapse using M_t and u^D_{rms}/u'. Furthermore, the M_t is not enough to characterize the flow compressibility of turbulence with large-scale thermal forcing. We need additional parameters (e.g. u^D_{rms}/u') to describe the statistical state of compressible turbulence. Donzis & John (2020) introduced a new parameter $\mathcal{D} \equiv \delta\sqrt{\delta^2+1}/M_t$, and suggested $\mathcal{D}$ as an appropriate parameter to determine the level of pressure fluctuation and the statistical regime of turbulence. Here, $\delta = u^D_{rms}/u^S_{rms}$. They noted that at high $\mathcal{D}$, the dilatational pressure dominated, and p-equipartition was the main mechanism governing the dynamics of pressure fluctuation; at low $\mathcal{D}$, the pressure was dominated by its elliptic nature dictated by the incompressible Navier–Stokes equations. The critical value $\mathcal{D}_{cr}$ approximately equals 0.5. The $\mathcal{D}$ values for present simulations are also included in tables 5–8. The $\mathcal{D} \approx 0.80$–1.48 for the $M_t \approx 0.22$ cases, while $\mathcal{D} \approx 0.23$–0.30 for the $M_t \approx 0.68$ cases. However, as mentioned above, the flow compressibility of the $M_t \approx 0.68$ cases is stronger than the $M_t \approx 0.22$ cases, although the p^D_{rms}/p^S_{rms} values are smaller in the $M_t \approx 0.68$ cases. There is an excellent collapse of the data based on the parameter $\mathcal{D}$ (as illustrated in figure 1(c) of Donzis & John (2020)); however, the parameter $\mathcal{D}$ may lead to some confusion about the statistical state of turbulence.

The universal scaling laws in compressible turbulence are extremely important, and we do appreciate the research works in Donzis & John (2020). However, as mentioned above, we need further investigations on the topic. Furthermore, fluctuations of the dilatational pressure and velocity components mainly come from large-scale motions, and, therefore, the validity of the weak form of acoustic equilibrium hypothesis does not imply the strong form. The validation of the strong form of acoustic equilibrium hypothesis will be discussed in § 4.

4. Dilatation and spectra of velocity and thermodynamic variables

The PDFs of normalized dilatation (θ/θ') for the $M_t \approx 0.22$ and 0.68 cases are shown in figure 1. As presented in figure 1(a), the PDFs of θ/θ' for cases I_1 and I_2 are negatively skewed. It indicates that in these two cases, the percentage of volume occupied by the strong compression region ($\theta/\theta' \leq -2.0$) is larger than its strong expansion counterpart ($\theta/\theta' \geq 2.0$). With the increase of $\langle K_\tau \rangle$, for case I_3, the PDF of θ/θ' is almost symmetrical about $\theta/\theta' = 0.0$. That is, the percentages of volume occupied by the strong compression and expansion regions are close to each other. Interestingly, the percentages of volume occupied by the strong compression and expansion regions are not monotonous with $\langle K_\tau \rangle$. As $\langle K_\tau \rangle$ further increases to 9.80 (case I_4), the PDF of θ/θ' is strongly skewed to the negative side. Furthermore, for cases I_5 and I_6, the strongly skewed PDFs are enhanced (figure 1a). For the $M_t \approx 0.68$ cases with different $\langle K_\tau \rangle$ and θ_v values, all PDFs of θ/θ' overlap roughly one another, being strongly skewed to the negative side (figure 1b). That is, for the $M_t \approx 0.68$ cases, the percentage of volume occupied by the strong compression region is larger than its strong expansion counterpart in despite of the vibrational relaxation effect.

To illustrate the effects of large-scale thermal forcing and vibrational relaxation on the compression and expansion motions in the presently simulated flows, the instantaneous isosurfaces and contours of θ/θ' for the $M_t \approx 0.22$ and 0.68 cases are illustrated in figures 2, 3, 4 and 5. As shown in figure 2(a,b), for cases I_2 and I_3, both the strong compression and expansion regions are fragmentized sheet-like structures. The fragmentized sheet-like structures are more clear in the instantaneous contours of θ/θ'

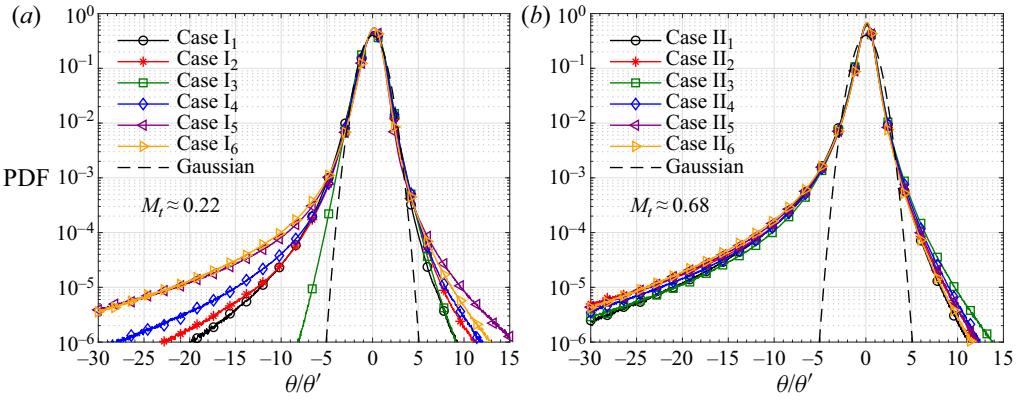

Figure 1. Probability density functions of normalized dilatation for (*a*) $M_t \approx 0.22$ and (*b*) $M_t \approx 0.68$ cases.

(figure 3*a*,*b*). It is a distinctive compressible turbulent structure which is not reported in the prior literature, and is attributed to the combined effects of large-scale thermal forcing and vibrational relaxation. In our previous work on compressible isotropic turbulence in vibrational non-equilibrium (Zheng *et al.* 2020), when the large-scale thermal forcing is excluded, both the strong compression and expansion regions are blob-like structures for the weakly compressible turbulence with $M_t \approx 0.44$. For case I_4 (figures 2*c* and 3*c*), as $\langle K_\tau \rangle$ increases to 9.80, the fragmentized sheet-like structures are replaced by the blob-like structures. In this case, the strong compression region is larger in size. For case I_6 (figures 2*d* and 3*d*), the flow compressibility is further enhanced. The percentage of volume occupied by the strong compression region is obviously larger than that by the strong expansion region. The structures in the former region are relatively flat and larger in size, while the latter region is characterized by the blob-like structures. For the $M_t \approx 0.68$ cases with different $\langle K_\tau \rangle$ and θ_v values, the instantaneous isosurfaces and contours of θ/θ' are similar (figures 4 and 5). In these cases, the strong compression and expansion regions are respectively populated by the 'shocklets' and blob-like structures.

As shown in figures 4 and 5, the strong compression structures in these cases are relatively thicker, compared with our previous results for $M_t \approx 1.0$ (Zheng *et al.* 2020). There is some literature about the estimation of shock thickness, such as Samtaney *et al.* (2001) and Donzis (2012). For example, Donzis (2012) mentioned that under laminar conditions, the normalized shock thickness could be written as

$$\frac{\delta_l}{\eta} \approx \frac{M_t}{Re_\lambda^{1/2} \Delta M}, \tag{4.1}$$

where $\Delta M = M - 1$ and η is the Kolmogorov scale. Under turbulent conditions, the shock thickness is essentially a random variable. The mean shock thickness can be given as

$$\frac{\langle \delta_l \rangle}{\eta} \approx \frac{M_t}{Re_\lambda^{1/2} \Delta M} \left[1 + \frac{1}{3} \frac{M_t^2}{\Delta M^2} + \cdots \right]. \tag{4.2}$$

However, the present observations reveal that for the compressible turbulence in vibrational non-equilibrium, the shock thickness is closely related to the vibrational relaxation. The approximate relationship between the shock thickness and other parameters (e.g. M_t, Re_λ and $\langle K_\tau \rangle$) is still not clear, and further investigations on the topic are required.

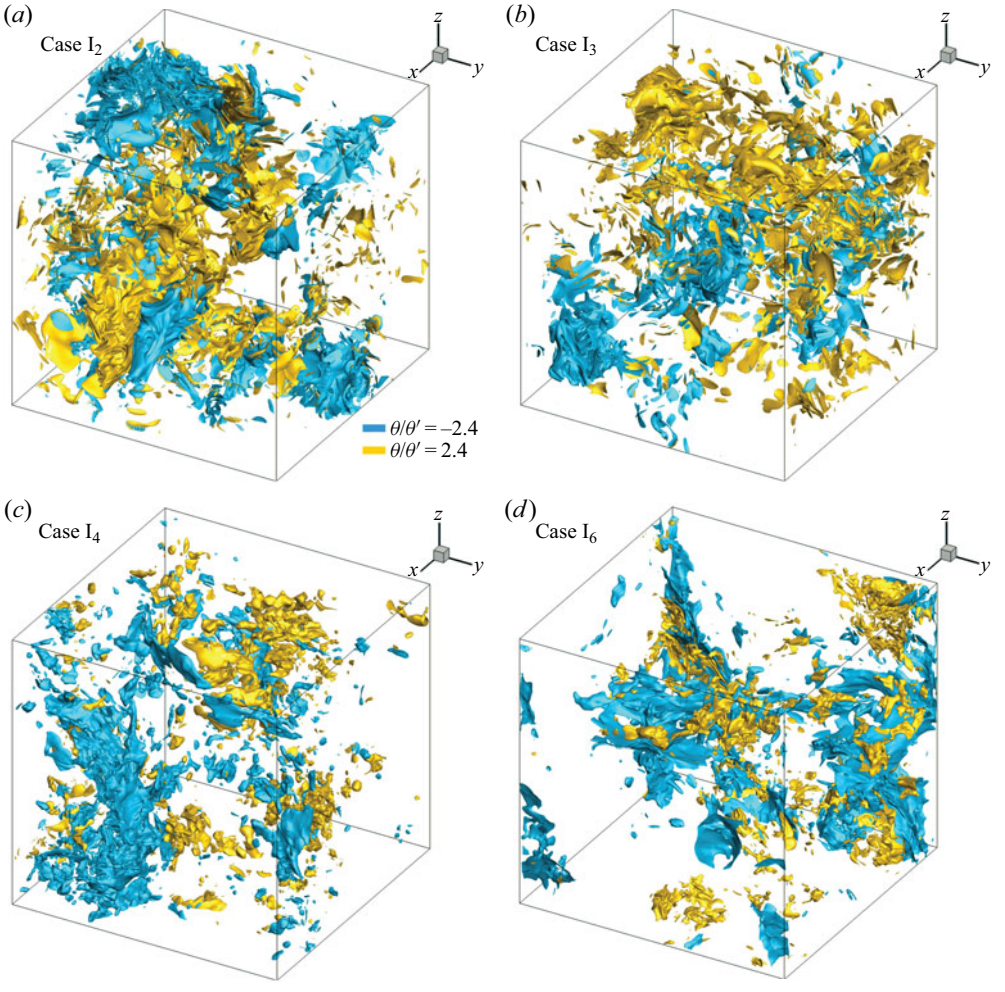

Figure 2. Instantaneous isosurfaces of normalized dilatation. (*a*) Case I_2, (*b*) case I_3, (*c*) case I_4 and (*d*) case I_6. Here $M_t \approx 0.22$.

Figure 6 illustrates the compensated velocity spectrum $E^u(k)\epsilon^{-2/3}k^{5/3}$ for the $M_t \approx 0.22$ and 0.68 cases, where the velocity spectrum $E^u(k)$ satisfies $\int_0^\infty E^u(k)\,\mathrm{d}k = \langle \boldsymbol{u}^2 \rangle/2$. An inertial range of the velocity spectrum is observed in the range of $0.05 \lesssim k\eta \lesssim 0.2$ with a plateau about 2.0, which is larger than the widely accepted Kolmogorov constant of approximately 1.6. This deviation may result from the 'bottleneck effect' due to the limited Re_λ (Gotoh & Fukayama 2001; Dobler *et al.* 2003). As mentioned in Donzis & Sreenivasan (2010), the spectral bump decreases slowly with Re_λ and became negligible only for Re_λ greater than $\mathcal{O}(10^5)$. Furthermore, the compensated spectra of density and temperatures (i.e. $E^\rho(k)k^{5/3}/(\rho)^2_{rms}$, $E^{T_{tr}}(k)k^{5/3}/(T_{tr})^2_{rms}$ and $E^{T_v}(k)k^{5/3}/(T_v)^2_{rms}$) are shown in figure 7, where $E^\rho(k)$, $E^{T_{tr}}(k)$ and $E^{T_v}(k)$ satisfy $\int_0^\infty E^\rho(k)\,\mathrm{d}k = (\rho)^2_{rms}$, $\int_0^\infty E^{T_{tr}}(k)\,\mathrm{d}k = (T_{tr})^2_{rms}$ and $\int_0^\infty E^{T_v}(k)\,\mathrm{d}k = (T_v)^2_{rms}$, respectively. The spectra of ρ, T_{tr} and T_v exhibit the $k^{-5/3}$ scaling for both the $M_t \approx 0.22$ and 0.68 cases; a plateau at intermediate wavenumbers is apparent. For the stationary compressible isotropic turbulence without vibrational excitation and large-scale thermal forcing (Donzis & Jagannathan 2013; Wang, Gotoh &

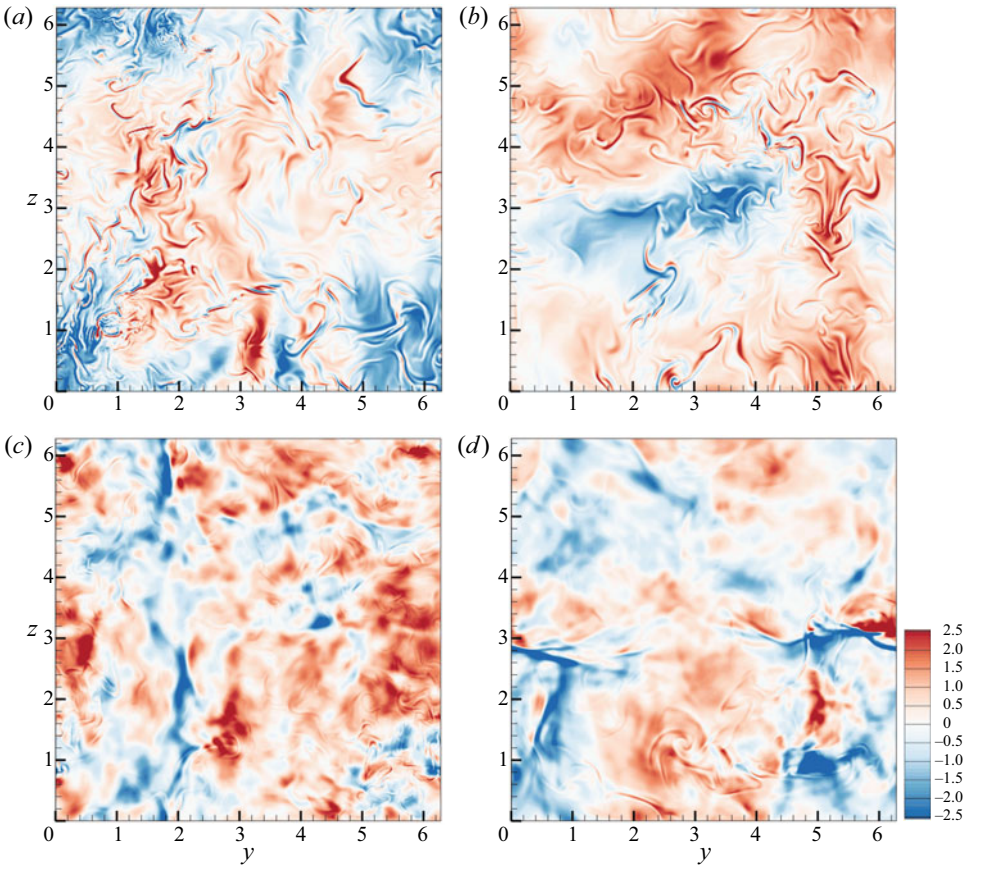

Figure 3. Instantaneous contours of normalized dilatation. (*a*) Case I_2, (*b*) case I_3, (*c*) case I_4 and (*d*) case I_6. Here $M_t \approx 0.22$.

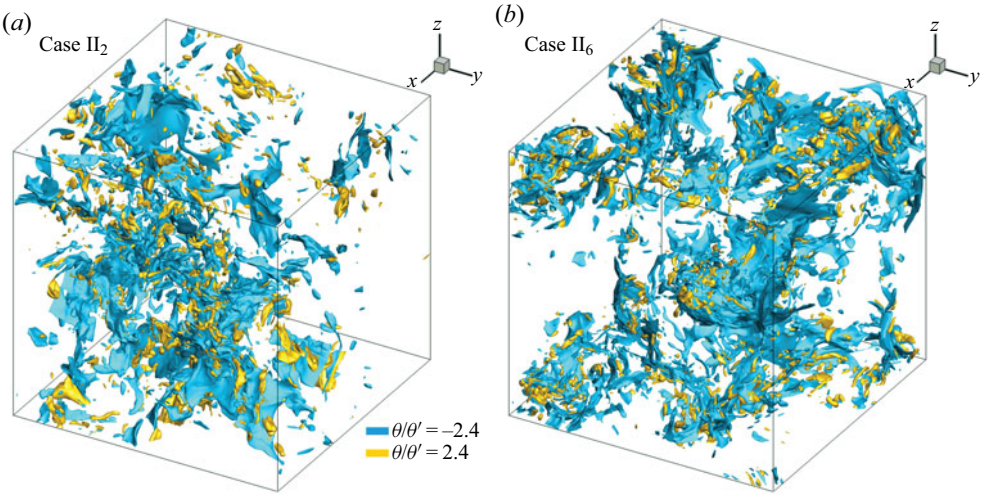

Figure 4. Instantaneous isosurfaces of normalized dilatation. (*a*) Case II_2, (*b*) case II_6. Here $M_t \approx 0.68$.

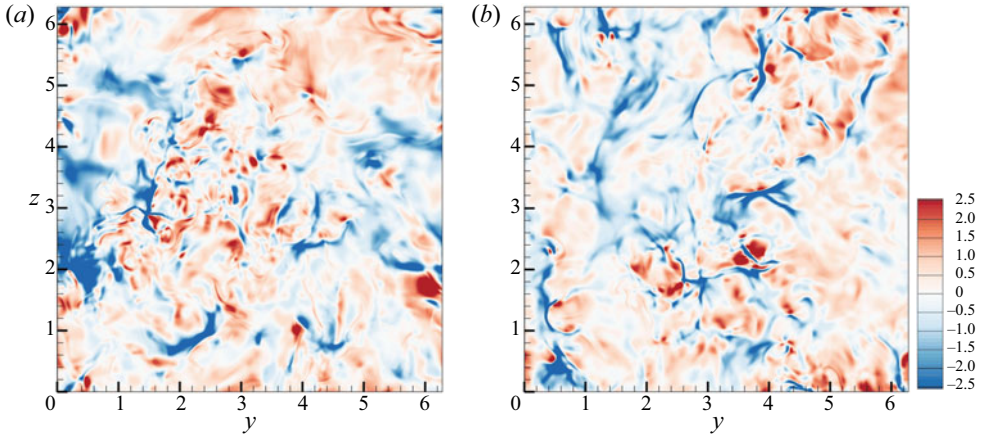

Figure 5. Instantaneous contours of normalized dilatation. (*a*) Case II_2, (*b*) case II_6. Here $M_t \approx 0.68$.

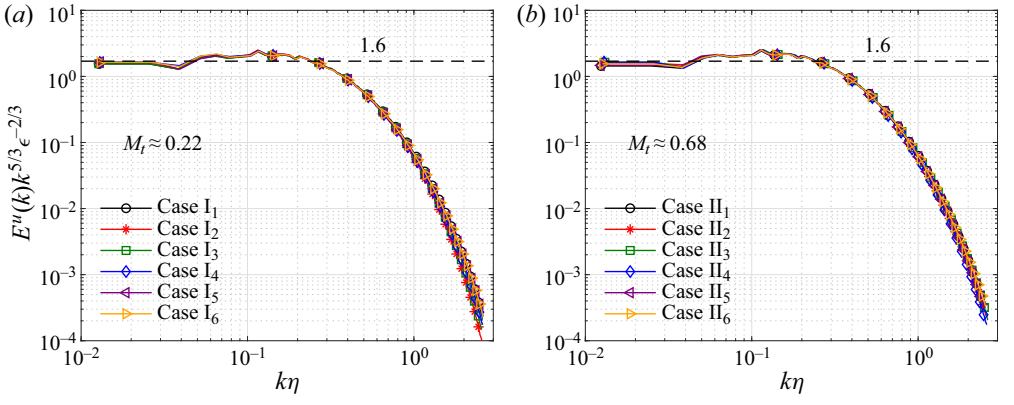

Figure 6. Compensated spectra of velocity for (*a*) $M_t \approx 0.22$ and (*b*) $M_t \approx 0.68$ cases.

Watanabe 2017), the pressure, density and temperature spectra follow a scale of $k^{-5/3}$ in a range of M_t. In addition, the fluctuations at high wavenumbers for the weakly compressible turbulence ($M_t \approx 0.1$) are much smaller than those for the highly compressible turbulence ($M_t \approx 0.6$), especially in the spectra of pressure and density. However, in the presently simulated flows the compensated spectra of density and temperature for the $M_t \approx 0.22$ and 0.68 cases are close to each other (figure 7), which suggests that the M_t effect is negligible. The difference with the observations by Donzis & Jagannathan (2013) and Wang *et al.* (2017) could be attributed to the fact that the large-scale thermal forcing enhances the flow compressibility and fluctuation of thermodynamic variables at high wavenumbers.

To reveal the effects of M_t, large-scale thermal forcing and vibrational relaxation on the pressure fluctuation, figure 8 presents the compensated spectra of pressure and its solenoidal and dilatational components. For both the $M_t \approx 0.22$ and 0.68 cases, the spectra of solenoidal pressure component overlap roughly each other, and exhibit a $k^{-5/3}$ scaling at intermediate wavenumbers. In other words, the fluctuation of solenoidal pressure component is almost insensitive to the effects of M_t, large-scale thermal forcing and vibrational relaxation. Note that, the $k^{-5/3}$ scaling for the spectrum of the solenoidal (incompressible) pressure component was observed in a large number of previous studies, such as Vedula & Yeung (1999), Gotoh & Rogallo (1999), Donzis

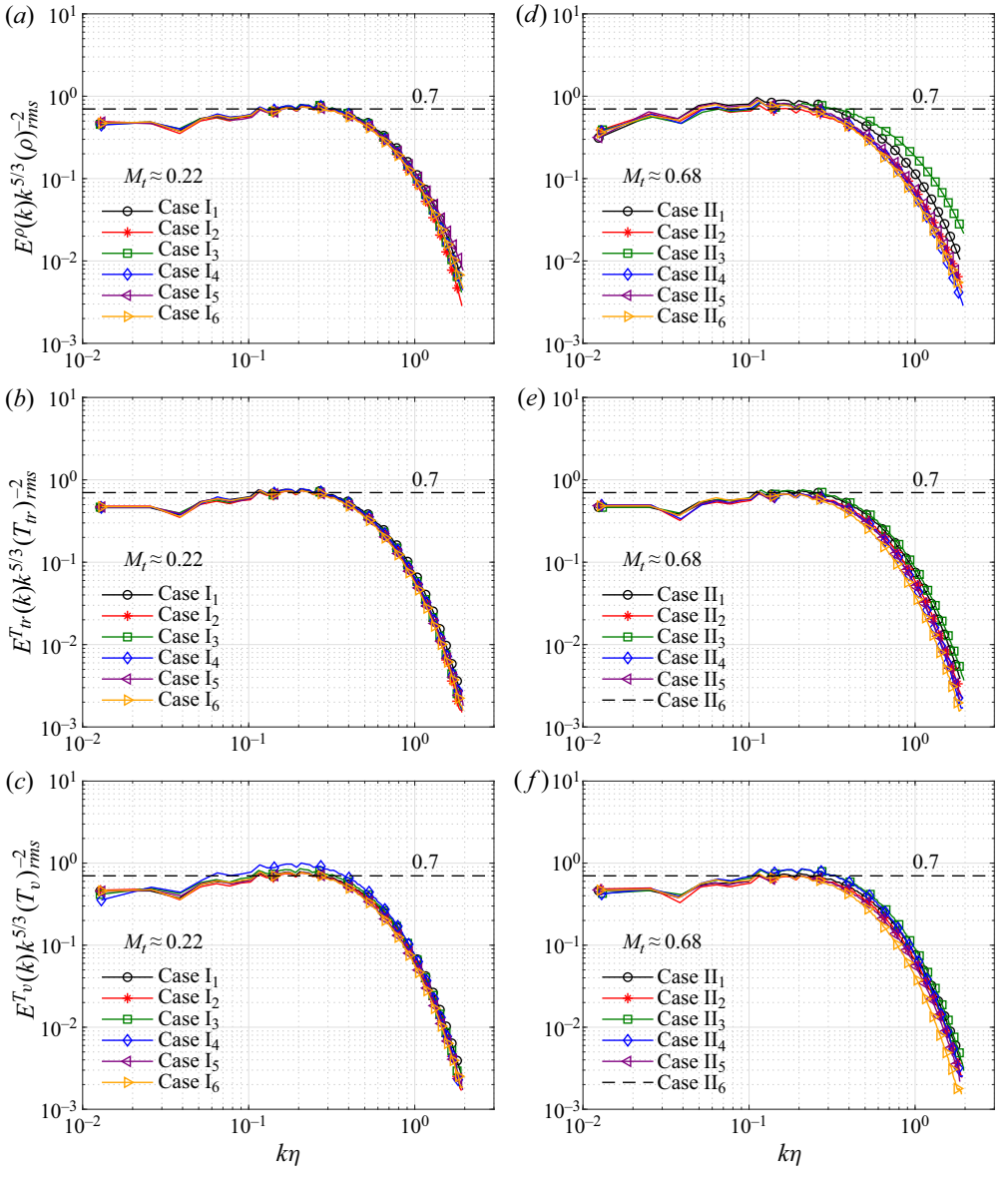

Figure 7. Compensated spectra of (*a*,*d*) density, (*b*,*e*) translational–rotational temperature and (*c*,*f*) vibrational temperature. Here, (*a–c*) $M_t \approx 0.22$ and (*d–f*) $M_t \approx 0.68$.

& Jagannathan (2013) and Wang *et al.* (2017). However, according to Kolmogorov's theory, the pressure spectrum in an incompressible turbulence should follow the $k^{-7/3}$ scaling. Gotoh & Fukayama (2001) suggested the $k^{-7/3}$ scaling with $Re_\lambda \geq 284$ in the numerical simulations of statistically steady homogeneous turbulence, while Tsuji & Ishihara (2003) found the $k^{-7/3}$ scaling with $Re_\lambda \geq 600$ in the experimental results of pressure fluctuation in a turbulent jet. Meldi & Sagaut (2013) further revealed that the $k^{-7/3}$ scaling could be observed only with $Re_\lambda = O(10^4)$ in the numerical simulations of freely decaying homogeneous isotropic turbulence. Wang *et al.* (2017) found the $k^{-7/3}$ scaling in the pressure spectrum at the beginning of the inertial range for the weakly

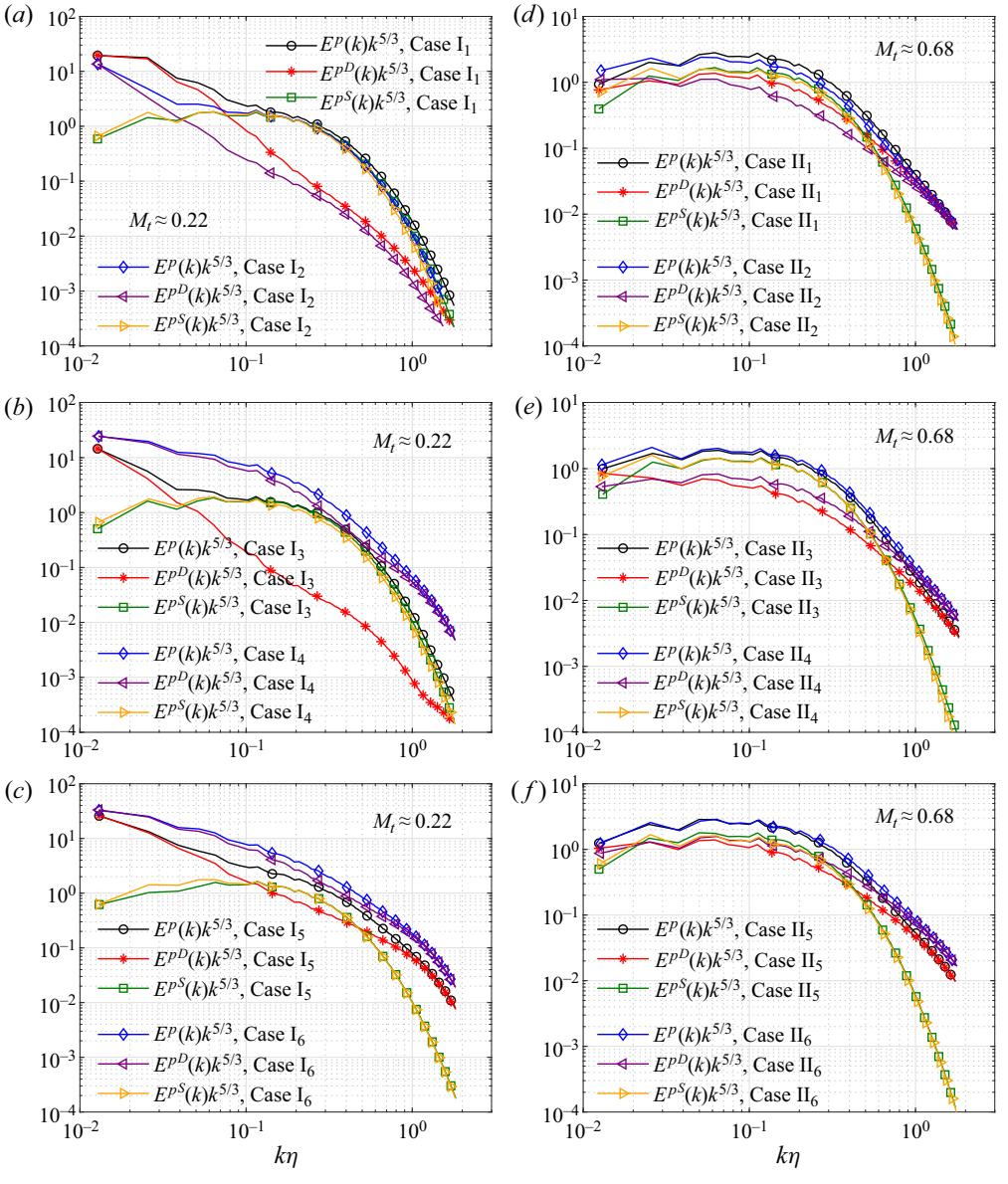

Figure 8. Compensated spectra of pressure and its solenoidal and dilatational components. Here, (*a–c*) $M_t \approx 0.22$ and (*d–f*) $M_t \approx 0.68$.

compressible isotropic turbulence with $M_t \leq 0.3$ and $Re_\lambda \approx 350$. Essentially, the exact threshold value of Re_λ for the $k^{-7/3}$ scaling is not confirmed, rather dependent on specific turbulence. The present $k^{-5/3}$ scaling for the spectra of solenoidal pressure component should be attributed to the finite-Reynolds-number effect ($Re_\lambda \approx 157.5$ for the present simulations).

For the $M_t \approx 0.22$ cases, because of the large-scale thermal forcing, the fluctuations of pressure and its dilatational component at low wavenumbers are much larger than their counterparts for the $M_t \approx 0.68$ cases (figure 8). For cases I$_1$–I$_3$, the fluctuations of pressure and its dilatational component do not differ much at low wavenumbers,

while the fluctuation of dilatational pressure component decreases sharply with increasing wavenumbers. The spectra of pressure and its solenoidal component overlap approximately in the range of $k\eta \geq 0.1$. In these cases, the fluctuation of pressure at intermediate and high wavenumbers is dominated by the solenoidal component (figure 8*a*,*b*). For cases I_4 ($\langle K_\tau \rangle = 9.80$), the fluctuation of pressure at full wavenumbers is largely dominated by the dilatational component, with a slight departure in the range of $0.1 \leq k/\eta \leq 0.7$. Furthermore, the fluctuation of pressure at high wavenumbers in this case is much larger than that in the former three cases (figure 8*b*). Similar observations are made for cases I_5 and I_6 (figure 8*c*). With the increase of θ_v, the fluctuations of pressure and its dilatational component at full wavenumbers increase, and the departure at intermediate wavenumbers shrinks. The above observations agree well with results in table 6, where p^D_{rms}/p^S_{rms} increases from 2.59 to 4.82 with θ_v varying from 1.0 to 5.0 (cases I_2, I_5, I_6). For the $M_t \approx 0.68$ cases, the large-scale thermal forcing does not increase the fluctuation of pressure or its dilatational component at low wavenumbers. At intermediate wavenumbers, the spectra of pressure and its dilatational component exhibit roughly the $k^{-5/3}$ scaling. The fluctuation of dilatational pressure component is comparable with the solenoidal component for case II_1 (figure 8*d*). As $\langle K_\tau \rangle$ increases from 0.19 to 7.98, the fluctuation of dilatational pressure component decreases gradually, which agrees well with the observation in table 7, where p^D_{rms}/p^S_{rms} decreases from 1.04 to 0.76 (cases II_1–II_4). For cases II_5 and II_6, the spectra of solenoidal and dilatational components overlap roughly each other at low and intermediate wavenumbers (figure 8*f*). Furthermore, different from the $M_t \approx 0.22$ cases, the fluctuation of pressure at high wavenumbers ($k\eta \geq 0.8$) is mainly dominated by the dilatational component for the $M_t \approx 0.68$ cases.

As mentioned in § 3, $\chi (= \langle p \rangle \gamma_r M_t (u^D_{rms}/u')/p^D_{rms})$ is close to 1.0 for both the $M_t \approx 0.22$ and 0.68 cases (tables 5–8), i.e. satisfying the weak form of acoustic equilibrium hypothesis. But how about the strong form of acoustic equilibrium hypothesis? Figure 9 presents the compensated spectra of dilatational velocity and pressure components (i.e. $2.0\gamma_r \langle \rho \rangle \langle p \rangle E^{u^D}(k)k^{-5/3}$ and $E^{p^D}(k)k^{-5/3}$) for the $M_t \approx 0.22$ and 0.68 cases. Obviously, the compensated spectra of dilatational velocity component are closely related to the vibrational relaxation for the $M_t \approx 0.22$ cases. For cases I_1–I_3, the two compensated spectra overlap at low wavenumbers, and begin to deviate at intermediate and high wavenumbers ($k\eta \geq 0.1$) (figure 9*a*). For cases I_4–I_6, although the two compensated spectra do not overlap exactly at intermediate and high wavenumbers, they are close to each other and their trends are consistent (figure 9*b*). It reveals that for the $M_t \approx 0.22$ cases, the strong acoustic equilibrium hypothesis is valid only at low wavenumbers when the vibrational relaxation effect is significant. When the vibrational relaxation effect weakens ($\langle K_\tau \rangle$ or θ_v is large enough), the strong acoustic equilibrium hypothesis is approximately valid at all wavenumbers. For the $M_t \approx 0.68$ cases with different $\langle K_\tau \rangle$ and θ_v values, the two compensated spectra almost collapse at all wavenumbers (figure 9*c*,*d*). The observations suggest that the strong acoustic equilibrium hypothesis is valid for the $M_t \approx 0.68$ cases in despite of the vibrational relaxation.

5. Dissipation of internal energy fluctuations

From (2.2) and (2.3), the governing equations for internal energy and its translational–rotational component per unit mass (e and e_{tr}) can be derived as

$$\frac{\partial \rho e}{\partial t} + \frac{\partial \rho e u_j}{\partial x_j} = \frac{1}{\alpha}\frac{\partial}{\partial x_j}\left(\kappa_{tr}\frac{\partial T_{tr}}{\partial x_j} + \kappa_v \frac{\partial T_v}{\partial x_j}\right) + \frac{1}{Re}\sigma_{ij}\frac{\partial u_i}{\partial x_j} - p\theta + \mathcal{F}_W, \tag{5.1}$$

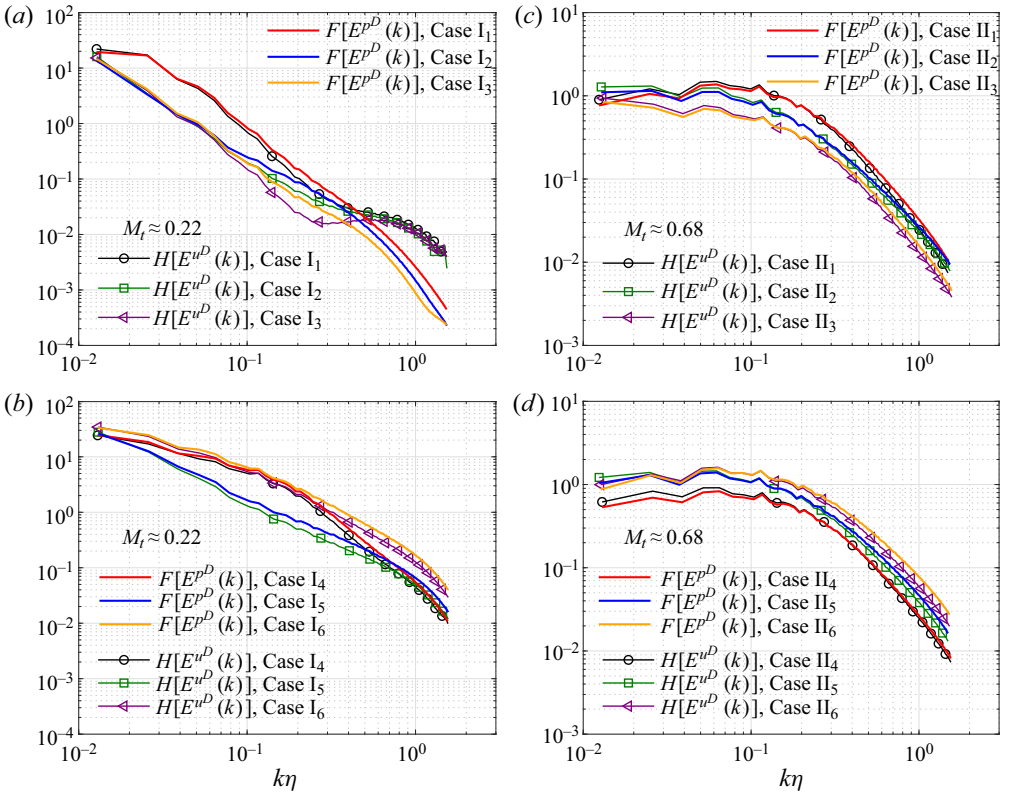

Figure 9. Compensated spectra of dilatational velocity and pressure components. Note that, $H[E^{u^D}(k)] = 2.0\gamma_r\langle\rho\rangle\langle p\rangle E^{u^D}(k)k^{-5/3}$, $F[E^{p^D}(k)] = E^{p^D}(k)k^{-5/3}$. Here, (*a*,*b*) $M_t \approx 0.22$ and (*c*,*d*) $M_t \approx 0.68$.

$$\frac{\partial \rho e_{tr}}{\partial t} + \frac{\partial \rho e_{tr} u_j}{\partial x_j} = \frac{1}{\alpha}\frac{\partial}{\partial x_j}\left(\kappa_{tr}\frac{\partial T_{tr}}{\partial x_j}\right) + \frac{1}{Re}\sigma_{ij}\frac{\partial u_i}{\partial x_j} - p\theta + \mathcal{F}_W - \frac{E_v^* - E_v}{\tau_v}, \tag{5.2}$$

where $\mathcal{F}_W = -\Lambda + \mathcal{F}_I$ represents effects of the cooling function and the large-scale thermal forcing.

The translational–rotational energy can be decomposed into a spatially averaged component $e_{tr_0}(=\langle e_{tr}\rangle)$ and a fluctuation component e_{tr_1}, i.e. $e_{tr} = e_{tr_0} + e_{tr_1}$. The governing equation for the variance of translational–rotational energy ($\langle e_{tr_1}^2\rangle$) can be derived by taking a dot product of the translational–rotational energy governing equation (5.2) with e_{tr_1} and spatially averaging, as

$$\frac{\partial\langle e_{tr_1}^2\rangle}{\partial t} = \left\langle (e_{tr_1}^2 - \frac{4}{5}e_{tr}e_{tr_1})\theta\right\rangle - \left\langle \kappa_{tr}\frac{\partial T_{tr}}{\partial x_j}\frac{\partial}{\partial x_j}\left(\frac{2e_{tr_1}}{\rho\alpha}\right)\right\rangle + \left\langle \frac{2e_{tr_1}}{Re\rho}\sigma_{ij}\frac{\partial u_i}{\partial x_j}\right\rangle$$
$$- \left\langle \frac{2e_{tr_1}}{\rho}\frac{E_v^* - E_v}{\tau_v}\right\rangle + \left\langle \frac{2e_{tr_1}}{\rho}F_W\right\rangle = -\langle \mathcal{C}_{e_{tr}}\rangle + \langle \mathcal{C}_{e_{tr}}^{inj}\rangle. \tag{5.3}$$

Here, the total change rate of translational–rotational energy fluctuation can be decomposed as $\langle \mathcal{C}_{e_{tr}}\rangle = \langle \mathcal{C}_{e_{tr}}^{\theta}\rangle + \langle \mathcal{C}_{e_{tr}}^{\kappa}\rangle + \langle \mathcal{C}_{e_{tr}}^{\mu}\rangle + \langle \mathcal{C}_{e_{tr}}^{\tau}\rangle$. The change rates due to the effects of dilatation, thermal conduction, viscosity and vibrational relaxation are respectively

Case	$\langle\mathcal{C}^{\theta}_{e_{tr}}\rangle/\langle\mathcal{C}_{e_{tr}}\rangle$	$\langle\mathcal{C}^{\kappa}_{e_{tr}}\rangle/\langle\mathcal{C}_{e_{tr}}\rangle$	$\langle\mathcal{C}^{\mu}_{e_{tr}}\rangle/\langle\mathcal{C}_{e_{tr}}\rangle$	$\langle\mathcal{C}^{\tau}_{e_{tr}}\rangle/\langle\mathcal{C}_{e_{tr}}\rangle$	$\langle\mathcal{C}^{\theta}_{e_v}\rangle/\langle-\mathcal{C}^{\tau}_{e_v}\rangle$	$\langle\mathcal{C}^{\kappa}_{e_v}\rangle/\langle-\mathcal{C}^{\tau}_{e_v}\rangle$
I_1	0.013	0.779	0.002	0.205	0.019	0.947
I_2	0.006	0.790	−0.004	0.208	−0.001	0.980
I_3	0.002	0.773	0.001	0.224	−0.030	1.015
I_4	0.006	0.763	0.000	0.232	−0.053	1.069

Table 9. The ratio of dissipation rates for translational–rotational and vibrational energy fluctuations. Considering $\langle K_\tau\rangle$ effects. Here $M_t \approx 0.22$.

Case	$\langle\mathcal{C}^{\theta}_{e_{tr}}\rangle/\langle\mathcal{C}_{e_{tr}}\rangle$	$\langle\mathcal{C}^{\kappa}_{e_{tr}}\rangle/\langle\mathcal{C}_{e_{tr}}\rangle$	$\langle\mathcal{C}^{\mu}_{e_{tr}}\rangle/\langle\mathcal{C}_{e_{tr}}\rangle$	$\langle\mathcal{C}^{\tau}_{e_{tr}}\rangle/\langle\mathcal{C}_{e_{tr}}\rangle$	$\langle\mathcal{C}^{\theta}_{e_v}\rangle/\langle-\mathcal{C}^{\tau}_{e_v}\rangle$	$\langle\mathcal{C}^{\kappa}_{e_v}\rangle/\langle-\mathcal{C}^{\tau}_{e_v}\rangle$
I_2	0.006	0.790	−0.004	0.208	−0.001	0.980
I_5	−0.011	0.870	0.001	0.141	0.009	1.035
I_6	−0.036	0.962	0.001	0.072	−0.057	0.936

Table 10. The ratio of dissipation rates for translational–rotational and vibrational energy fluctuations. Considering θ_v effects. Here $M_t \approx 0.22$.

denoted as

$$\langle\mathcal{C}^{\theta}_{e_{tr}}\rangle = -\left\langle(e^2_{tr_1} - \frac{4}{5}e_{tr}e_{tr_1})\theta\right\rangle, \quad \langle\mathcal{C}^{\kappa}_{e_{tr}}\rangle = \left\langle\kappa_{tr}\frac{\partial T_{tr}}{\partial x_j}\frac{\partial}{\partial x_j}\left(\frac{2e_{tr_1}}{\rho\alpha}\right)\right\rangle, \tag{5.4a,b}$$

$$\langle\mathcal{C}^{\mu}_{e_{tr}}\rangle = -\left\langle\frac{2e_{tr_1}}{Re\rho}\sigma_{ij}\frac{\partial u_i}{\partial x_j}\right\rangle \quad \text{and} \quad \langle\mathcal{C}^{\tau}_{e_{tr}}\rangle = \left\langle\frac{2e_{tr_1}}{\rho}\frac{E^*_v - E_v}{\tau_v}\right\rangle. \tag{5.5a,b}$$

The $\langle\mathcal{C}^{inj}_{e_{tr}}\rangle = \langle(2e_{tr_1}/\rho)F_W\rangle$ represents the injection of translational–rotational energy fluctuation by the cooling function and large-scale thermal forcing.

Similarly, the governing equation for the variance of vibrational energy is derived as

$$\frac{\partial\langle e^2_{v_1}\rangle}{\partial t} = \langle e^2_{v_1}\theta\rangle - \left\langle\kappa_v\frac{\partial T_v}{\partial x_j}\frac{\partial}{\partial x_j}\left(\frac{2e_{v_1}}{\rho\alpha}\right)\right\rangle + \left\langle\frac{2e_{v_1}}{\rho}\frac{E^*_v - E_v}{\tau_v}\right\rangle = -\langle\mathcal{C}_{e_v}\rangle, \tag{5.6}$$

where $e_{v_1} = e_v - e_{v_0}$ and $e_{v_0} = \langle e_v\rangle$. The total change rate of vibrational energy fluctuation is decomposed as $\langle\mathcal{C}_{e_v}\rangle = \langle\mathcal{C}^{\theta}_{e_v}\rangle + \langle\mathcal{C}^{\kappa}_{e_v}\rangle + \langle\mathcal{C}^{\tau}_{e_v}\rangle$. The change rates due to the effects of dilatation, thermal conduction and vibrational relaxation are respectively

$$\langle\mathcal{C}^{\theta}_{e_v}\rangle = -\langle e^2_{v_1}\theta\rangle, \quad \langle\mathcal{C}^{\kappa}_{e_v}\rangle = \left\langle\kappa_v\frac{\partial T_v}{\partial x_j}\frac{\partial}{\partial x_j}\left(\frac{2e_{v_1}}{\rho\alpha}\right)\right\rangle \quad \text{and} \quad \langle\mathcal{C}^{\tau}_{e_v}\rangle = -\left\langle\frac{2e_{v_1}}{\rho}\frac{E^*_v - E_v}{\tau_v}\right\rangle. \tag{5.7a–c}$$

The change rates of the translational–rotational and vibrational energy fluctuations are given in tables 9 and 10 for the $M_t \approx 0.22$ cases, and in tables 11 and 12 for the $M_t \approx 0.68$ cases. The total change rates of the translational–rotational and vibrational energy fluctuations for the $M_t \approx 0.22$ and 0.68 cases are given in table 13. For the translational–rotational energy fluctuation, from (5.3), the total change rate $\langle\mathcal{C}_{e_{tr}}\rangle$ is positive. As shown in tables 9–12, $\langle\mathcal{C}^{\theta}_{e_{tr}}\rangle/\langle\mathcal{C}_{e_{tr}}\rangle$ and $\langle\mathcal{C}^{\mu}_{e_{tr}}\rangle/\langle\mathcal{C}_{e_{tr}}\rangle$ are negligibly small, while $\langle\mathcal{C}^{\kappa}_{e_{tr}}\rangle/\langle\mathcal{C}_{e_{tr}}\rangle$ is larger than $\langle\mathcal{C}^{\tau}_{e_{tr}}\rangle/\langle\mathcal{C}_{e_{tr}}\rangle$. It suggests that for both the $M_t \approx 0.22$ and 0.68 cases, on spatial average, the change rates of translational–rotational energy fluctuation due to the dilatation and viscosity are negligible; the dissipation mainly comes from the

Case	$\langle \mathcal{C}^{\theta}_{e_{tr}} \rangle / \langle \mathcal{C}_{e_{tr}} \rangle$	$\langle \mathcal{C}^{\kappa}_{e_{tr}} \rangle / \langle \mathcal{C}_{e_{tr}} \rangle$	$\langle \mathcal{C}^{\mu}_{e_{tr}} \rangle / \langle \mathcal{C}_{e_{tr}} \rangle$	$\langle \mathcal{C}^{\tau}_{e_{tr}} \rangle / \langle \mathcal{C}_{e_{tr}} \rangle$	$\langle \mathcal{C}^{\theta}_{e_{v}} \rangle / \langle -\mathcal{C}^{\tau}_{e_{v}} \rangle$	$\langle \mathcal{C}^{\kappa}_{e_{v}} \rangle / \langle -\mathcal{C}^{\tau}_{e_{v}} \rangle$
II_1	−0.028	0.757	−0.007	0.277	0.117	0.874
II_2	−0.083	0.751	−0.017	0.349	0.097	0.891
II_3	−0.081	0.788	−0.020	0.314	−0.013	1.001
II_4	0.024	0.706	−0.011	0.280	−0.075	1.062

Table 11. The ratio of dissipation rates for translational–rotational and vibrational energy fluctuations. Considering $\langle K_\tau \rangle$ effects. Here $M_t \approx 0.68$.

Case	$\langle \mathcal{C}^{\theta}_{e_{tr}} \rangle / \langle \mathcal{C}_{e_{tr}} \rangle$	$\langle \mathcal{C}^{\kappa}_{e_{tr}} \rangle / \langle \mathcal{C}_{e_{tr}} \rangle$	$\langle \mathcal{C}^{\mu}_{e_{tr}} \rangle / \langle \mathcal{C}_{e_{tr}} \rangle$	$\langle \mathcal{C}^{\tau}_{e_{tr}} \rangle / \langle \mathcal{C}_{e_{tr}} \rangle$	$\langle \mathcal{C}^{\theta}_{e_{v}} \rangle / \langle -\mathcal{C}^{\tau}_{e_{v}} \rangle$	$\langle \mathcal{C}^{\kappa}_{e_{v}} \rangle / \langle -\mathcal{C}^{\tau}_{e_{v}} \rangle$
II_2	−0.083	0.751	−0.017	0.349	0.097	0.891
II_5	0.054	0.735	0.003	0.207	0.060	0.882
II_6	0.105	0.790	0.016	0.089	−0.048	1.056

Table 12. The ratio of dissipation rates for translational–rotational and vibrational energy fluctuations. Considering θ_v effects. Here $M_t \approx 0.68$.

Case	$\langle \mathcal{C}_{e_{tr}} \rangle$	$\langle \mathcal{C}^{\tau}_{e_{v}} \rangle$	Case	$\langle \mathcal{C}_{e_{tr}} \rangle$	$\langle \mathcal{C}^{\tau}_{e_{v}} \rangle$
I_1	1117.00	−79.09	II_1	13.05	−0.95
I_2	994.24	−69.69	II_2	10.88	−0.76
I_3	1035.40	−65.55	II_3	11.66	−0.71
I_4	1073.70	−58.27	II_4	11.86	−0.62
I_5	913.20	−20.56	II_5	12.18	−0.25
I_6	829.71	−3.11	II_6	11.67	−0.04

Table 13. Total change rates of translational–rotational and change rate of vibrational energy fluctuations due to vibrational relaxation for the $M_t \approx 0.22$ and 0.68 cases.

effects of thermal conduction and vibrational relaxation, while the former plays a major role. As shown in table 13, $\langle \mathcal{C}_{e_{tr}} \rangle$ and $\langle \mathcal{C}_{e_v} \rangle$ for the $M_t \approx 0.22$ cases are much larger than their counterparts for the $M_t \approx 0.68$ cases. It implies that the large-scale thermal forcing has more significant impacts for the $M_t \approx 0.22$ cases, which agrees well with the observations in § 4.

For the $M_t \approx 0.22$ cases, $\langle \mathcal{C}^{\kappa}_{e_{tr}} \rangle / \langle \mathcal{C}_{e_{tr}} \rangle$ keeps almost constant (≈ 0.776, table 9) for cases I_1–I_4, and increases from 0.790 to 0.962 with θ_v varying from 1.0 to 5.0 (cases $\mathrm{I}_2, \mathrm{I}_5, \mathrm{I}_6$, table 10). Furthermore, $\langle \mathcal{C}^{\tau}_{e_{tr}} \rangle / \langle \mathcal{C}_{e_{tr}} \rangle$ increases slightly from 0.205 to 0.232 as $\langle K_\tau \rangle$ increases from 0.16 to 9.80, while decreasing sharply from 0.208 to 0.072 with θ_v varying from 1.0 to 5.0. For the $M_t \approx 0.68$ cases, $\langle \mathcal{C}^{\kappa}_{e_{tr}} \rangle / \langle \mathcal{C}_{e_{tr}} \rangle \approx 0.739$ for different cases (tables 11 and 12). The $\langle \mathcal{C}^{\tau}_{e_{tr}} \rangle / \langle \mathcal{C}_{e_{tr}} \rangle \approx 0.277$ with $\langle K_\tau \rangle \approx 0.19$. The $\langle \mathcal{C}^{\tau}_{e_{tr}} \rangle / \langle \mathcal{C}_{e_{tr}} \rangle$ wanes from 0.349 to 0.280 as $\langle K_\tau \rangle$ increases from 0.86 to 7.98 (table 11), and declines sharply from 0.349 to 0.089 with θ_v varying from 1.0 to 5.0 (table 12). Note that, for the $M_t \approx 0.68$ cases, the dilatation term also plays a considerable role with increasing θ_v; for instance, $\langle \mathcal{C}^{\theta}_{e_{tr}} \rangle / \langle \mathcal{C}_{e_{tr}} \rangle$ is about 0.105 for case II_6. The observations indicate that the variation of $\langle \mathcal{C}^{\kappa}_{e_{tr}} \rangle / \langle \mathcal{C}_{e_{tr}} \rangle$ depends mainly on θ_v for the $M_t \approx 0.22$ cases, and is almost insensitive to $\langle K_\tau \rangle$ and θ_v for the $M_t \approx 0.68$ cases. Furthermore, for both the $M_t \approx 0.22$ and 0.68 cases, $\langle \mathcal{C}^{\tau}_{e_{tr}} \rangle / \langle \mathcal{C}_{e_{tr}} \rangle$ has a limited connection with $\langle K_\tau \rangle$, while highly depends on θ_v. As θ_v increases, the dissipation of translational–rotational energy fluctuation due to the vibrational relaxation loses its significance rapidly.

For the vibrational energy fluctuation (5.6), the total change rate $\langle \mathcal{C}_{e_v} \rangle$ approximately equals zero. Because of the equilibrium departure, an exchange between the translational–rotational and vibrational energies takes place via vibrational relaxation. Consequently, the change rate due to the vibrational relaxation ($\langle \mathcal{C}^{\tau}_{e_v} \rangle$) is negative (table 13). That is, the vibrational relaxation enhances essentially the vibrational energy fluctuation. From tables 9–12, $\langle \mathcal{C}^{\theta}_{e_v} \rangle / (-\langle \mathcal{C}^{\tau}_{e_v} \rangle)$ roughly equals 0.0, while $\langle \mathcal{C}^{\kappa}_{e_v} \rangle / (-\langle \mathcal{C}^{\tau}_{e_v} \rangle)$ is close to 1.0. It suggests that the change rate of vibrational energy fluctuation due to the dilatation is nearly negligible, while the dissipation of vibrational energy fluctuation due to the thermal conduction is roughly equivalent to the production owing to the vibrational relaxation.

To investigate the effect of flow compressibility on the change rate of internal energy fluctuations, we define the parameters

$$\mathcal{C}^{\theta}_{e_{tr}} = -\left(e^2_{tr_1} - \frac{4}{5} e_{tr} e_{tr_1}\right)\theta, \quad \mathcal{C}^{\kappa}_{e_{tr}} = \kappa_{tr} \frac{\partial T_{tr}}{\partial x_j} \frac{\partial}{\partial x_j}\left(\frac{2e_{tr_1}}{\rho\alpha}\right), \tag{5.8a,b}$$

$$\mathcal{C}^{\mu}_{e_{tr}} = -\frac{2e_{tr_1}}{Re\rho}\sigma_{ij}\frac{\partial u_i}{\partial x_j} \quad \text{and} \quad \mathcal{C}^{\tau}_{e_{tr}} = \frac{2e_{tr_1}}{\rho}\frac{E^*_v - E_v}{\tau_v}, \tag{5.9a,b}$$

for the translational–rotational energy fluctuation, and

$$\mathcal{C}^{\theta}_{e_v} = -e^2_{v_1}\theta, \quad \mathcal{C}^{\kappa}_{e_v} = \kappa_v \frac{\partial T_v}{\partial x_j}\frac{\partial}{\partial x_j}\left(\frac{2e_{v_1}}{\rho\alpha}\right) \quad \text{and} \quad \mathcal{C}^{\tau}_{e_v} = -\frac{2e_{v_1}}{\rho}\frac{E^*_v - E_v}{\tau_v}, \tag{5.10a–c}$$

for the vibrational energy fluctuation. The spatially averaged $(\mathcal{C}^{\theta}_{e_{tr}} - \langle \mathcal{C}^{\theta}_{e_{tr}} \rangle)/\langle \mathcal{C}_{e_{tr}} \rangle$, $(\mathcal{C}^{\kappa}_{e_{tr}} - \langle \mathcal{C}^{\kappa}_{e_{tr}} \rangle)/\langle \mathcal{C}_{e_{tr}} \rangle$, $(\mathcal{C}^{\mu}_{e_{tr}} - \langle \mathcal{C}^{\mu}_{e_{tr}} \rangle)/\langle \mathcal{C}_{e_{tr}} \rangle$, $(\mathcal{C}^{\tau}_{e_{tr}} - \langle \mathcal{C}^{\tau}_{e_{tr}} \rangle)/\langle \mathcal{C}_{e_{tr}} \rangle$, $(\mathcal{C}^{\theta}_{e_v} - \langle \mathcal{C}^{\theta}_{e_v} \rangle)/(-\langle \mathcal{C}^{\tau}_{e_v} \rangle)$, $(\mathcal{C}^{\kappa}_{e_v} - \langle \mathcal{C}^{\kappa}_{e_v} \rangle)/(-\langle \mathcal{C}^{\tau}_{e_v} \rangle)$ and $(\mathcal{C}^{\tau}_{e_v} - \langle \mathcal{C}^{\tau}_{e_v} \rangle)/(-\langle \mathcal{C}^{\tau}_{e_v} \rangle)$ conditioned on θ/θ' are presented in figure 10. Here, only the $M_t \approx 0.68$ cases are considered owing to their notable flow compressibility.

For the fluctuation of translational–rotational energy, as shown in figure 10(*a*), the $\langle (\mathcal{C}^{\theta}_{e_{tr}} - \langle \mathcal{C}^{\theta}_{e_{tr}} \rangle)/\langle \mathcal{C}_{e_{tr}} \rangle | \theta/\theta' \rangle$ is positive and increases rapidly in the compression region, while it is negative and decreases sharply in the expansion region. Note that in the range of $|\theta/\theta'| \leq 0.65$, the changes of $\langle (\mathcal{C}^{\theta}_{e_{tr}} - \langle \mathcal{C}^{\theta}_{e_{tr}} \rangle)/\langle \mathcal{C}_{e_{tr}} \rangle | \theta/\theta' \rangle$ are relatively small. Compared with the dilatation term, the dependence of other terms on θ/θ' is much weaker. The $\langle (\mathcal{C}^{\kappa}_{e_{tr}} - \langle \mathcal{C}^{\kappa}_{e_{tr}} \rangle)/\langle \mathcal{C}_{e_{tr}} \rangle | \theta/\theta' \rangle$ rises with the increase of θ/θ' magnitude in the compression and expansion regions (figure 10*b*). In the strong compression region ($\theta/\theta' \leq -2.0$), it is insensitive to $\langle K_\tau \rangle$, but enlarges with the increase of θ_v. Beyond the strong compression region, the vibrational relaxation effect is negligibly small. For the $\langle (\mathcal{C}^{\mu}_{e_{tr}} - \langle \mathcal{C}^{\mu}_{e_{tr}} \rangle)/\langle \mathcal{C}_{e_{tr}} \rangle | \theta/\theta' \rangle$, the effects of flow compressibility and vibrational relaxation are weak. The $\langle (\mathcal{C}^{\mu}_{e_{tr}} - \langle \mathcal{C}^{\mu}_{e_{tr}} \rangle)/\langle \mathcal{C}_{e_{tr}} \rangle | \theta/\theta' \rangle$ for different cases roughly overlap each other and keep almost constant in the compression and expansion regions (figure 10*b*). Here, to distinguish the thermal conduction term from the viscosity term, the solid lines representing $\langle (\mathcal{C}^{\mu}_{e_{tr}} - \langle \mathcal{C}^{\mu}_{e_{tr}} \rangle)/\langle \mathcal{C}_{e_{tr}} \rangle | \theta/\theta' \rangle$ are offset by -1.0. For the $\langle (\mathcal{C}^{\tau}_{e_{tr}} - \langle \mathcal{C}^{\tau}_{e_{tr}} \rangle)/\langle \mathcal{C}_{e_{tr}} \rangle | \theta/\theta' \rangle$, their variances in the compression region are closely related to the vibrational relaxation. The $\langle (\mathcal{C}^{\tau}_{e_{tr}} - \langle \mathcal{C}^{\tau}_{e_{tr}} \rangle)/\langle \mathcal{C}_{e_{tr}} \rangle | \theta/\theta' \rangle$ are close for cases II_1 and II_2, being positive and enlarging with the increase of θ/θ' magnitude in the compression region. The magnitude of $\langle (\mathcal{C}^{\tau}_{e_{tr}} - \langle \mathcal{C}^{\tau}_{e_{tr}} \rangle)/\langle \mathcal{C}_{e_{tr}} \rangle | \theta/\theta' \rangle$ is significantly suppressed with the increase of $\langle K_\tau \rangle$ and θ_v (figure 10*c*). For example, for cases II_3 and II_4, the $\langle (\mathcal{C}^{\tau}_{e_{tr}} - \langle \mathcal{C}^{\tau}_{e_{tr}} \rangle)/\langle \mathcal{C}_{e_{tr}} \rangle | \theta/\theta' \rangle$ is almost insensitive to θ/θ'. In the expansion region, however, no obvious dependence on the flow compressibility and vibrational relaxation is observed.

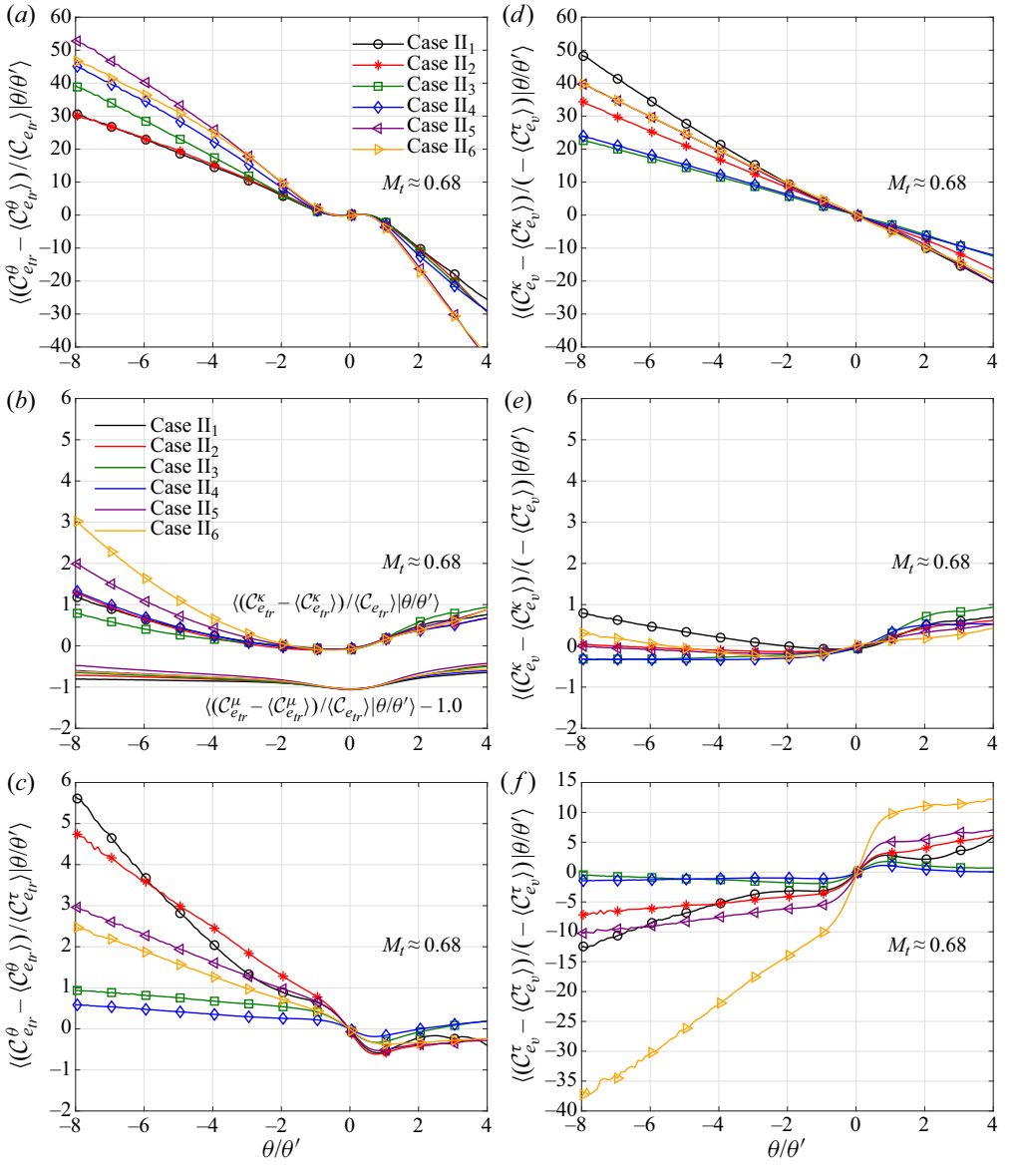

Figure 10. Spatially averaged (*a*) $(\mathcal{C}^{\theta}_{e_{tr}} - \langle\mathcal{C}^{\theta}_{e_{tr}}\rangle)/\langle\mathcal{C}_{e_{tr}}\rangle$, (*b*) $(\mathcal{C}^{\kappa}_{e_{tr}} - \langle\mathcal{C}^{\kappa}_{e_{tr}}\rangle)/\langle\mathcal{C}_{e_{tr}}\rangle$ (with symbol), $(\mathcal{C}^{\mu}_{e_{tr}} - \langle\mathcal{C}^{\mu}_{e_{tr}}\rangle)/\langle\mathcal{C}_{e_{tr}}\rangle$ (solid line), (*c*) $(\mathcal{C}^{\tau}_{e_{tr}} - \langle\mathcal{C}^{\tau}_{e_{tr}}\rangle)/\langle\mathcal{C}_{e_{tr}}\rangle$, (*d*) $(\mathcal{C}^{\theta}_{e_v} - \langle\mathcal{C}^{\theta}_{e_v}\rangle)/(-\langle\mathcal{C}^{\tau}_{e_v}\rangle)$, (*e*) $(\mathcal{C}^{\kappa}_{e_v} - \langle\mathcal{C}^{\kappa}_{e_v}\rangle)/(-\langle\mathcal{C}^{\tau}_{e_v}\rangle)$ and (*f*) $(\mathcal{C}^{\tau}_{e_v} - \langle\mathcal{C}^{\tau}_{e_v}\rangle)/(-\langle\mathcal{C}^{\tau}_{e_v}\rangle)$ conditioned on θ/θ'. $M_t \approx 0.68$.

For the vibrational energy fluctuation, the $\langle(\mathcal{C}^{\theta}_{e_v} - \langle\mathcal{C}^{\theta}_{e_v}\rangle)/(-\langle\mathcal{C}^{\tau}_{e_v}\rangle)|\theta/\theta'\rangle$ for different cases are positive and negative in the compression and expansion regions, respectively (figure 10*d*). Their magnitudes are amplified with the increase of θ/θ' magnitude. The $\langle(\mathcal{C}^{\kappa}_{e_v} - \langle\mathcal{C}^{\kappa}_{e_v}\rangle)/(-\langle\mathcal{C}^{\tau}_{e_v}\rangle)|\theta/\theta'\rangle$ for different cases are insensitive to θ/θ' and vibrational relaxation, keeping constant in the compression region except case II_1, while increasing slightly in the expansion region (figure 10*e*). As shown in figure 10(*f*), the $\langle(\mathcal{C}^{\tau}_{e_v} - \langle\mathcal{C}^{\tau}_{e_v}\rangle)/(-\langle\mathcal{C}^{\tau}_{e_v}\rangle)|\theta/\theta'\rangle$ are close for cases II_1 and II_2, being negative in the

compression region and positive in the expansion region. The dependence of $\langle(\mathcal{C}^{\tau}_{e_v} - \langle\mathcal{C}^{\tau}_{e_v}\rangle)/(-\langle\mathcal{C}^{\tau}_{e_v}\rangle)|\theta/\theta'\rangle$ on the flow compressibility reduces greatly as $\langle K_\tau\rangle$ increases. For instance, the $\langle(\mathcal{C}^{\tau}_{e_v} - \langle\mathcal{C}^{\tau}_{e_v}\rangle)/(-\langle\mathcal{C}^{\tau}_{e_v}\rangle)|\theta/\theta'\rangle$ is almost insensitive to the compressibility for cases II_3 and II_4. Note that, the dependency of $\langle(\mathcal{C}^{\tau}_{e_v} - \langle\mathcal{C}^{\tau}_{e_v}\rangle)/(-\langle\mathcal{C}^{\tau}_{e_v}\rangle)|\theta/\theta'\rangle$ is enhanced sharply for case II_6, because the value of $(-\langle\mathcal{C}^{\tau}_{e_v}\rangle)$ for case II_6 is much smaller than other cases (table 13).

6. Transfer of internal energy fluctuation

The Favre filtering approach is employed to study the transfers of translational–rotational and vibrational energy fluctuations. The classically filtered field $\bar{f}$ is defined as $\bar{f}(\boldsymbol{x}) \equiv \int \mathrm{d}^3\boldsymbol{r} G_l(\boldsymbol{r}) f(\boldsymbol{x}+\boldsymbol{r})$. The $G_l(\boldsymbol{r}) \equiv l^{-3}G(\boldsymbol{r}/l)$ is the filter function, where $G(\boldsymbol{r})$ is a normalized window function and l is the filter width. The Favre filtered field $\tilde{f}$ is defined as $\tilde{f} \equiv \overline{\rho f}/\bar{\rho}$. In the present study a top-hat filter is adopted, which is calculated by (Martin, Piomelli & Candler 2000)

$$\bar{f}_i = \frac{1}{4n}\left(f_{i-n} + 2\sum_{j=i-n+1}^{i+n-1} f_j + f_{i+n}\right), \tag{6.1}$$

where the filter width $l = 2n\Delta x$.

The governing equation for the variance of filtered translational–rotational energy can be derived from (5.2) as

$$\begin{aligned}\frac{\partial\langle\tilde{e}^2_{tr_1}\rangle}{\partial t} &= \left\langle\tilde{e}^2_{tr_1}\theta_l - \frac{2\tilde{e}_{tr_1}}{\bar{\rho}}\overline{p\theta}\right\rangle - \left\langle\overline{\kappa_{tr}\frac{\partial T_{tr}}{\partial x_j}}\frac{\partial}{\partial x_j}\left(\frac{2\tilde{e}_{tr_1}}{\bar{\rho}\alpha}\right)\right\rangle + \left\langle\frac{2\tilde{e}_{tr_1}}{Re\bar{\rho}}\overline{\sigma_{ij}\frac{\partial u_i}{\partial x_j}}\right\rangle \\ &\quad - \left\langle\frac{2\tilde{e}_{tr_1}}{\bar{\rho}}\overline{\frac{E^*_v - E_v}{\tau_v}}\right\rangle + \left\langle\bar{\rho}(\widetilde{e_{tr_1}u_j} - \tilde{e}_{tr_1}\tilde{u}_j)\frac{\partial}{\partial x_j}\left(\frac{2\tilde{e}_{tr_1}}{\bar{\rho}}\right)\right\rangle + \left\langle\frac{2\tilde{e}_{tr_1}}{\bar{\rho}}\bar{F}_W\right\rangle \\ &= -\langle\Phi^{e_{tr}}_l + D^{e_{tr}}_l + \Gamma^{e_{tr}}_l + \Pi^{e_{tr}}_l\rangle + \langle F^{e_{tr}}_l\rangle,\end{aligned} \tag{6.2}$$

where $\theta_l(=\partial\tilde{u}_j/\partial x_j)$ is the filtered velocity divergence. The dilatation term $\Phi^{e_{tr}}_l$, thermal conduction and viscosity term $D^{e_{tr}}_l$, vibrational relaxation term $\Gamma^{e_{tr}}_l$, subgrid-scale (SGS) flux term $\Pi^{e_{tr}}_l$, and effects of large-scale thermal forcing and cooling function $F^{e_{tr}}_l$ can be respectively presented as

$$\Phi^{e_{tr}}_l = -\tilde{e}^2_{tr_1}\theta_l + \frac{2\tilde{e}_{tr_1}}{\bar{\rho}}\overline{p\theta}, \quad D^{e_{tr}}_l = \overline{\kappa_{tr}\frac{\partial T_{tr}}{\partial x_j}}\frac{\partial}{\partial x_j}\left(\frac{2\tilde{e}_{tr_1}}{\bar{\rho}\alpha}\right) - \frac{2\tilde{e}_{tr_1}}{Re\bar{\rho}}\overline{\sigma_{ij}\frac{\partial u_i}{\partial x_j}}, \tag{6.3a,b}$$

$$\Gamma^{e_{tr}}_l = \frac{2\tilde{e}_{tr_1}}{\bar{\rho}}\overline{\frac{E^*_v - E_v}{\tau_v}}, \quad \Pi^{e_{tr}}_l = -\bar{\rho}(\widetilde{e_{tr_1}u_j} - \tilde{e}_{tr_1}\tilde{u}_j)\frac{\partial}{\partial x_j}\left(\frac{2\tilde{e}_{tr_1}}{\bar{\rho}}\right) \tag{6.4a,b}$$

$$\text{and} \quad F^{e_{tr}}_l = \frac{2\tilde{e}_{tr_1}}{\bar{\rho}}\bar{F}_W. \tag{6.5}$$

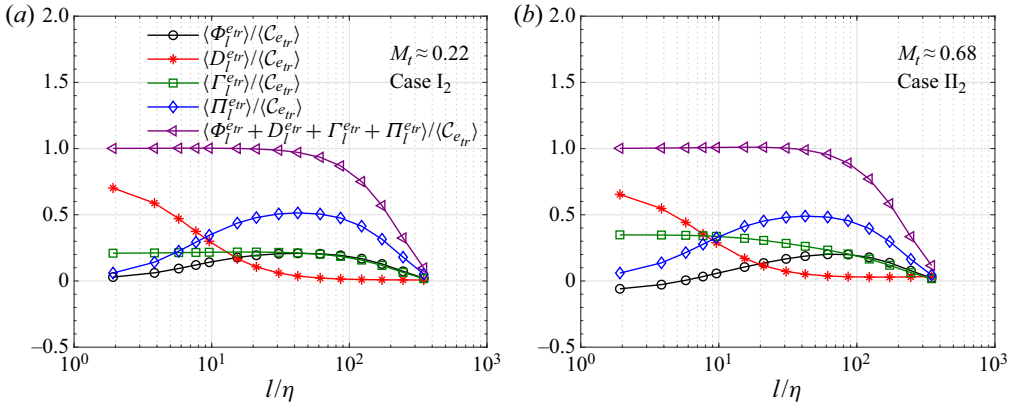

Figure 11. Dependence on l/η of $\langle \Phi_l^{e_{tr}} \rangle / \langle \mathcal{C}_{e_{tr}} \rangle$, $\langle D_l^{e_{tr}} \rangle / \langle \mathcal{C}_{e_{tr}} \rangle$, $\langle \Gamma_l^{e_{tr}} \rangle / \langle \mathcal{C}_{e_{tr}} \rangle$, $\langle \Pi_l^{e_{tr}} \rangle / \langle \mathcal{C}_{e_{tr}} \rangle$ and $\langle \Phi_l^{e_{tr}} + D_l^{e_{tr}} + \Gamma_l^{e_{tr}} + \Pi_l^{e_{tr}} \rangle / \langle \mathcal{C}_{e_{tr}} \rangle$. (*a*) Case I_2, (*b*) case II_2.

Similarly, the governing equation for the variance of filtered vibrational energy can be derived from (2.4) as

$$\frac{\partial \langle \tilde{e}_{v_1}^2 \rangle}{\partial t} = \langle \tilde{e}_{v_1}^2 \theta_l \rangle - \left\langle \overline{\kappa_v \frac{\partial T_v}{\partial x_j}} \frac{\partial}{\partial x_j} \left(\frac{2\tilde{e}_{v_1}}{\bar{\rho}\alpha} \right) \right\rangle + \left\langle \frac{2\tilde{e}_{v_1}}{\bar{\rho}} \frac{\overline{E_v^* - E_v}}{\tau_v} \right\rangle + \left\langle \bar{\rho} (\widetilde{e_{v_1} u_j} - \tilde{e}_{v_1} \tilde{u}_j) \frac{\partial}{\partial x_j} \left(\frac{2\tilde{e}_{v_1}}{\bar{\rho}} \right) \right\rangle = -\langle \Phi_l^{e_v} + D_l^{e_v} + \Gamma_l^{e_v} + \Pi_l^{e_v} \rangle. \tag{6.6}$$

The dilatation term $\Phi_l^{e_v}$, thermal conduction term $D_l^{e_v}$, vibrational relaxation term $\Gamma_l^{e_v}$ and SGS flux term $\Pi_l^{e_v}$ can be respectively denoted as

$$\Phi_l^{e_v} = -\tilde{e}_{v_1}^2 \theta_l, \quad D_l^{e_v} = \overline{\kappa_v \frac{\partial T_v}{\partial x_j}} \frac{\partial}{\partial x_j} \left(\frac{2\tilde{e}_{v_1}}{\bar{\rho}\alpha} \right), \tag{6.7a,b}$$

$$\Gamma_l^{e_v} = -\frac{2\tilde{e}_{v_1}}{\bar{\rho}} \frac{\overline{E_v^* - E_v}}{\tau_v} \quad \text{and} \quad \Pi_l^{e_v} = -\bar{\rho} (\widetilde{e_{v_1} u_j} - \tilde{e}_{v_1} \tilde{u}_j) \frac{\partial}{\partial x_j} \left(\frac{2\tilde{e}_{v_1}}{\bar{\rho}} \right). \tag{6.8a,b}$$

6.1. *Transfer of internal energy fluctuation*

The dependence of $\langle \Phi_l^{e_{tr}} + D_l^{e_{tr}} + \Gamma_l^{e_{tr}} + \Pi_l^{e_{tr}} \rangle / \langle \mathcal{C}_{e_{tr}} \rangle$, $\langle \Phi_l^{e_{tr}} \rangle / \langle \mathcal{C}_{e_{tr}} \rangle$, $\langle D_l^{e_{tr}} \rangle / \langle \mathcal{C}_{e_{tr}} \rangle$, $\langle \Gamma_l^{e_{tr}} \rangle / \langle \mathcal{C}_{e_{tr}} \rangle$ and $\langle \Pi_l^{e_{tr}} \rangle / \langle \mathcal{C}_{e_{tr}} \rangle$ on l/η are similar among the $M_t \approx 0.22$ cases. So are the $M_t \approx 0.68$ cases. Here, as shown in figure 11, the cases I_2 and II_2 are taken to be examples. The $\langle \Phi_l^{e_{tr}} + D_l^{e_{tr}} + \Gamma_l^{e_{tr}} + \Pi_l^{e_{tr}} \rangle / \langle \mathcal{C}_{e_{tr}} \rangle$ approximately equals 1.0 in the range of $l/\eta \leq 50.0$ (figure 11*a*,*b*). It indicates that the effect of large-scale forcing on the transfer of translational–rotational energy fluctuation is mainly localized in large-scale motions. The $\langle \Phi_l^{e_{tr}} \rangle / \langle \mathcal{C}_{e_{tr}} \rangle$ increases in the range of $l/\eta \leq 50.0$ and decreases in $l/\eta > 50.0$ for case I_2. Similarly, $\langle \Phi_l^{e_{tr}} \rangle / \langle \mathcal{C}_{e_{tr}} \rangle$ increases in $l/\eta \leq 70.0$ and decreases in $l/\eta > 70.0$ for case II_2. The observation suggests that on spatial average, the dilatation effect weakens the translational–rotational energy fluctuation in large-scale motions, and enhances it in small- and intermediate-scale motions. The $\langle D_l^{e_{tr}} \rangle / \langle \mathcal{C}_{e_{tr}} \rangle$ approximately equals 0.7 and 0.65 at $l/\eta \approx 1.92$ for cases I_2 and II_2, respectively, and decreases monotonously with l/η. The $\langle D_l^{e_{tr}} \rangle / \langle \mathcal{C}_{e_{tr}} \rangle$ approaches 0.0 in $l/\eta \geq 60.0$ (figure 11*a*,*b*). That is, the thermal

conduction and viscosity effects weaken the translational–rotational energy fluctuation, and mainly act on small- and intermediate-scale motions. The $\langle \Gamma_l^{e_{tr}} \rangle / \langle \mathcal{C}_{e_{tr}} \rangle$ keeps constant ($\approx$0.2) in $l/\eta \leq 60.0$ for case I_2, and $\approx$0.35 in $l/\eta \leq 7.0$ for case II_2 (figure 11*a*,*b*), and reduces with l/η beyond these ranges. It implies that the vibrational relaxation weakens the translational–rotational energy fluctuation, and acts mainly on large-scale motions for the $M_t \approx 0.22$ cases. The affected range is extended to intermediate- and large-scale motions for the $M_t \approx 0.68$ cases. Furthermore, the vibrational relaxation effect on the dissipation of translational–rotational energy fluctuation is stronger in the $M_t \approx 0.68$ cases. This observation is consistent with the results in tables 9–12, where $\langle \mathcal{C}_{e_{tr}}^{\tau} \rangle / \langle \mathcal{C}_{e_{tr}} \rangle$ values for the $M_t \approx 0.22$ cases are always smaller than their counterparts for the $M_t \approx 0.68$ cases. As shown in figure 11(*a*,*b*), $\langle \Pi_l^{e_{tr}} \rangle / \langle \mathcal{C}_{e_{tr}} \rangle \approx 0.5$ in $20 \leq l/\eta \leq 80$ for cases I_2 and II_2, suggesting that about half of the translational–rotational energy fluctuations cascade from large- to small-scale motions in this range. Obviously, in this range ($20 \leq l/\eta \leq 80$), the dilatation and vibrational relaxation terms (i.e. $\langle \Phi_l^{e_{tr}} \rangle / \langle \mathcal{C}_{e_{tr}} \rangle$ and $\langle \Pi_l^{e_{tr}} \rangle / \langle \mathcal{C}_{e_{tr}} \rangle$) also play a significant role, and dissipate another half of the translational–rotational energy fluctuation. These observations are different from the previous results about cascades of thermal parameters in the compressible isotropic turbulence without vibrational excitation. Wang *et al.* (2019) investigated the cascades of temperature and entropy fluctuations of the stationary compressible isotropic turbulence with large-scale thermal forcing in the absence of vibrational relaxation. They found that $\langle \Pi_l^T \rangle / \epsilon_T \approx 1.0$ and $\langle \Pi_l^s \rangle / \epsilon_s \approx 1.0$ in $30 \leq l/\eta \leq 100$ for both the $M_t \approx 0.2$ and 0.6 cases. That is, all of the temperature and entropy fluctuations cascade approximately from large- to small-scale motions in this range, while the dilatation term plays a negligible role in dissipating the temperature and entropy fluctuations.

Figure 12 shows the dependence on l/η of $\langle \Phi_l^{e_v} + D_l^{e_v} + \Gamma_l^{e_v} + \Pi_l^{e_v} \rangle / (-\langle \mathcal{C}_{e_v}^{\tau} \rangle)$, $\langle \Phi_l^{e_v} \rangle / (-\langle \mathcal{C}_{e_v}^{\tau} \rangle)$, $\langle D_l^{e_v} \rangle / (-\langle \mathcal{C}_{e_v}^{\tau} \rangle)$, $\langle \Gamma_l^{e_v} \rangle / (-\langle \mathcal{C}_{e_v}^{\tau} \rangle)$ and $\langle \Pi_l^{e_v} \rangle / (-\langle \mathcal{C}_{e_v}^{\tau} \rangle)$ for cases I_2 and II_2. As mentioned in § 5, for the vibrational energy fluctuation, the vibrational relaxation would be a production term, i.e. $\langle \mathcal{C}_{e_v}^{\tau} \rangle < 0.0$ (table 13). In figure 12, $(-\langle \mathcal{C}_{e_v}^{\tau} \rangle)$ is thus selected to be the denominator. The $\langle \Gamma_l^{e_v} \rangle / (-\langle \mathcal{C}_{e_v}^{\tau} \rangle) \approx -1.0$ in $l/\eta \leq 60.0$ suggests that the effect of vibrational relaxation is mainly localized in large-scale motions, enhancing the vibrational energy fluctuation. From (6.6), $\langle \Phi_l^{e_v} + D_l^{e_v} + \Gamma_l^{e_v} + \Pi_l^{e_v} \rangle / (-\langle \mathcal{C}_{e_v}^{\tau} \rangle) \approx 0.0$ is expected (figure 12*a*,*b*). Furthermore, different from the transfer of translational–rotational energy fluctuation, the dilatation effect on the vibrational energy fluctuation in different scale motions is insignificant. The $\langle \Phi_l^{e_v} \rangle / (-\langle \mathcal{C}_{e_v}^{\tau} \rangle) \approx 0.0$ with different l/η values for cases I_2 and II_2. The $\langle D_l^{e_v} \rangle / (-\langle \mathcal{C}_{e_v}^{\tau} \rangle)$ approximately equals 0.87 and 0.79 at $l/\eta \approx 1.92$ for cases I_2 and II_2, respectively. The $\langle D_l^{e_v} \rangle / (-\langle \mathcal{C}_{e_v}^{\tau} \rangle)$ dwindles monotonously with l/η, and approaches 0.0 at $l/\eta \approx 60.0$ (figure 12*a*,*b*). That is, the thermal conduction effect weakens the vibrational energy fluctuation, and acts mainly on small- and intermediate-scale motions. For cases I_2 and II_2, $\langle \Pi_l^{e_v} \rangle / (-\langle \mathcal{C}_{e_v}^{\tau} \rangle) \approx 1.0$ in $20 \leq l/\eta \leq 80$ suggests that most of the vibrational energy fluctuations cascade from large- to small-scale motions in this range.

6.2. *Components of the SGS flux term*

The SGS fluxes of translational–rotational energy fluctuation based on the solenoidal and dilatational velocity components can be respectively derived as

$$\Pi_l^{e_{tr},S} = -\bar{\rho}(\widetilde{e_{tr_1} u_j^S} - \tilde{e}_{tr_1} \tilde{u}_j^S) \frac{\partial}{\partial x_j} \left(\frac{2\tilde{e}_{tr_1}}{\bar{\rho}} \right) \tag{6.9}$$

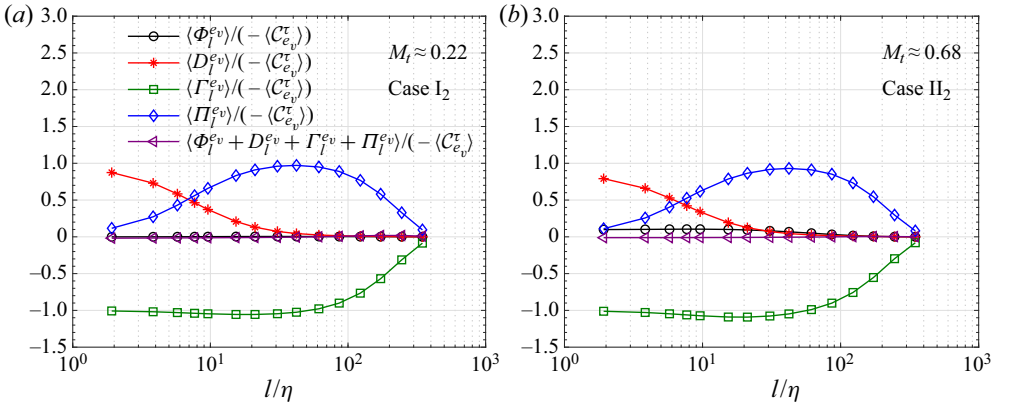

Figure 12. Dependence on l/η of $\langle \Phi_l^{e_v} \rangle / (-\langle \mathcal{C}_{e_v}^{\tau} \rangle)$, $\langle D_l^{e_v} \rangle / (-\langle \mathcal{C}_{e_v}^{\tau} \rangle)$, $\langle \Gamma_l^{e_v} \rangle / (-\langle \mathcal{C}_{e_v}^{\tau} \rangle)$, $\langle \Pi_l^{e_v} \rangle / (-\langle \mathcal{C}_{e_v}^{\tau} \rangle)$ and $\langle \Phi_l^{e_v} + D_l^{e_v} + \Gamma_l^{e_v} + \Pi_l^{e_v} \rangle / (-\langle \mathcal{C}_{e_v}^{\tau} \rangle)$. (*a*) Case I_2, (*b*) case II_2.

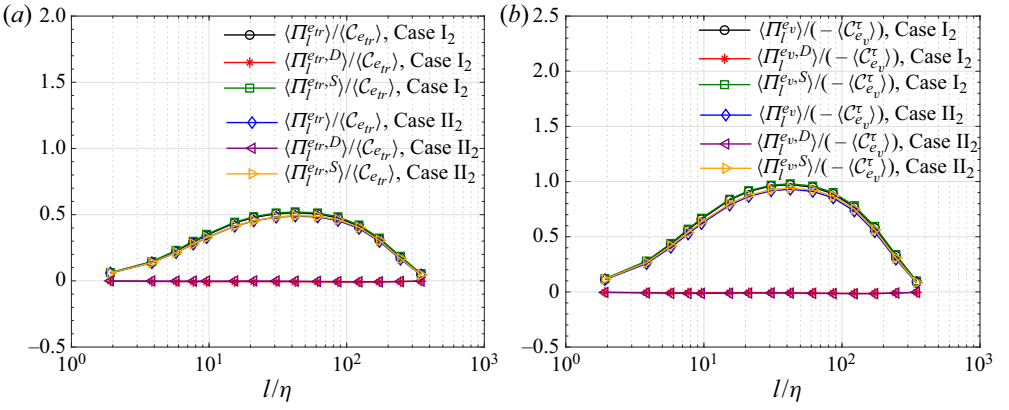

Figure 13. Spatially averaged SGS fluxes (including dilatational and solenoidal components) of (*a*) translational–rotational energy fluctuation and (*b*) vibrational energy fluctuation.

and

$$\Pi_l^{e_{tr},D} = -\bar{\rho}(\widetilde{e_{tr_1} u_j^D} - \tilde{e}_{tr_1} \tilde{u}_j^D) \frac{\partial}{\partial x_j} \left(\frac{2\tilde{e}_{tr_1}}{\bar{\rho}} \right). \tag{6.10}$$

Similarly, the SGS fluxes of vibrational energy fluctuation based on the solenoidal and dilatational velocity components are respectively

$$\Pi_l^{e_v,S} = -\bar{\rho}(\widetilde{e_{v_1} u_j^S} - \tilde{e}_{v_1} \tilde{u}_j^S) \frac{\partial}{\partial x_j} \left(\frac{2\tilde{e}_{v_1}}{\bar{\rho}} \right) \tag{6.11}$$

and

$$\Pi_l^{e_v,D} = -\bar{\rho}(\widetilde{e_{v_1} u_j^D} - \tilde{e}_{v_1} \tilde{u}_j^D) \frac{\partial}{\partial x_j} \left(\frac{2\tilde{e}_{v_1}}{\bar{\rho}} \right). \tag{6.12}$$

Note that, $\widetilde{\boldsymbol{u}}^D$ and $\widetilde{\boldsymbol{u}}^S$ are the dilatational and solenoidal components of filtered velocity $\widetilde{\boldsymbol{u}}$, respectively. Figure 13 illustrates the spatially averaged SGS fluxes of translational–rotational and vibrational energy fluctuations based on the solenoidal

Case	$\langle \Pi_l^{e_{tr}} \rangle^*$	$\langle \Pi_l^{e_{tr},S} \rangle^*$	$\langle \Pi_l^{e_v} \rangle^\dagger$	$\langle \Pi_l^{e_v,S} \rangle^\dagger$	Case	$\langle \Pi_l^{e_{tr}} \rangle^*$	$\langle \Pi_l^{e_{tr},S} \rangle^*$	$\langle \Pi_l^{e_v} \rangle^\dagger$	$\langle \Pi_l^{e_v,S} \rangle^\dagger$
I_1	0.429	0.438	0.815	0.829	II_1	0.426	0.436	0.788	0.806
I_2	0.437	0.443	0.833	0.840	II_2	0.413	0.414	0.787	0.799
I_3	0.431	0.442	0.817	0.827	II_3	0.440	0.460	0.829	0.857
I_4	0.421	0.427	0.800	0.794	II_4	0.384	0.379	0.835	0.847

Table 14. Spatially averaged SGS fluxes of translational–rotational and vibrational energy fluctuations at $l/\eta \approx 15.37$. Here $\langle\cdot\rangle^* = \langle\cdot\rangle/\langle \mathcal{C}_{e_{tr}} \rangle$ and $\langle\cdot\rangle^\dagger / = \langle\cdot\rangle/(-\langle \mathcal{C}_{e_v}^\tau \rangle)$. Considering $\langle K_\tau \rangle$ effects.

Case	$\langle \Pi_l^{e_{tr}} \rangle^*$	$\langle \Pi_l^{e_{tr},S} \rangle^*$	$\langle \Pi_l^{e_v} \rangle^\dagger$	$\langle \Pi_l^{e_v,S} \rangle^\dagger$	Case	$\langle \Pi_l^{e_{tr}} \rangle^*$	$\langle \Pi_l^{e_{tr},S} \rangle^*$	$\langle \Pi_l^{e_v} \rangle^\dagger$	$\langle \Pi_l^{e_v,S} \rangle^\dagger$
I_2	0.437	0.443	0.833	0.840	II_2	0.413	0.414	0.787	0.799
I_5	0.468	0.480	0.825	0.822	II_5	0.408	0.406	0.775	0.777
I_6	0.525	0.547	0.732	0.728	II_6	0.423	0.405	0.872	0.839

Table 15. Spatially averaged SGS fluxes of translational–rotational and vibrational energy fluctuations at $l/\eta \approx 15.37$. Here $\langle\cdot\rangle^* = \langle\cdot\rangle/\langle \mathcal{C}_{e_{tr}} \rangle$ and $\langle\cdot\rangle^\dagger / = \langle\cdot\rangle/(-\langle \mathcal{C}_{e_v}^\tau \rangle)$. Considering θ_v effects.

and dilatational velocity components for cases I_2 and II_2. Interestingly, it is found that $\langle \Pi_l^{e_{tr},D} \rangle/\langle \mathcal{C}_{e_{tr}} \rangle \approx 0.0$, $\langle \Pi_l^{e_v,D} \rangle/(-\langle \mathcal{C}_{e_v}^\tau \rangle) \approx 0.0$, $\langle \Pi_l^{e_{tr},S} \rangle/\langle \mathcal{C}_{e_{tr}} \rangle \approx \langle \Pi_l^{e_{tr}} \rangle/\langle \mathcal{C}_{e_{tr}} \rangle$ and $\langle \Pi_l^{e_v,S} \rangle/(-\langle \mathcal{C}_{e_v}^\tau \rangle) \approx \langle \Pi_l^{e_v} \rangle/(-\langle \mathcal{C}_{e_v}^\tau \rangle)$ with different l/η values for cases I_2 and II_2 (figure 13). The observation suggests that the spatially averaged SGS fluxes of translational–rotational and vibrational energy fluctuations are mainly dominated by the solenoidal velocity component.

To discuss the effects of M_t and vibrational relaxation on the transfer of internal energy fluctuation, the spatially averaged SGS fluxes at $l/\eta \approx 15.37$ are presented in tables 14 and 15 for both the $M_t \approx 0.22$ and 0.68 cases. The spatially averaged SGS fluxes are normalized by $\langle \mathcal{C}_{e_{tr}} \rangle$ for the translational–rotational energy fluctuation, and by $-\langle \mathcal{C}_{e_v}^\tau \rangle$ for the vibrational energy fluctuation. Here, $\langle \Pi_l^{e_{tr},D} \rangle/\langle \mathcal{C}_{e_{tr}} \rangle$ and $\langle \Pi_l^{e_v,D} \rangle/(-\langle \mathcal{C}_{e_v}^\tau \rangle)$ approximately equal 0.0, and are not presented in tables 14 and 15 for brevity. Obviously, the results agree well with the observations of figure 13: $\langle \Pi_l^{e_{tr}} \rangle/\langle \mathcal{C}_{e_{tr}} \rangle$ and $\langle \Pi_l^{e_v} \rangle/(-\langle \mathcal{C}_{e_v}^\tau \rangle)$ are respectively close to $\langle \Pi_l^{e_{tr},S} \rangle/\langle \mathcal{C}_{e_{tr}} \rangle$ and $\langle \Pi_l^{e_v,S} \rangle/(-\langle \mathcal{C}_{e_v}^\tau \rangle)$ for all cases. For the $M_t \approx 0.22$ cases, $\langle \Pi_l^{e_{tr}} \rangle/\langle \mathcal{C}_{e_{tr}} \rangle$ is insensitive to $\langle K_\tau \rangle$, but depends on θ_v. The $\langle \Pi_l^{e_{tr}} \rangle/\langle \mathcal{C}_{e_{tr}} \rangle$ is about 0.430 as $\langle K_\tau \rangle$ increases from 0.16 to 9.80, and enlarges slightly from 0.437 to 0.525 with θ_v varying from 1.0 to 5.0. For the $M_t \approx 0.68$ cases, $\langle \Pi_l^{e_{tr}} \rangle/\langle \mathcal{C}_{e_{tr}} \rangle$ is insensitive to both $\langle K_\tau \rangle$ and θ_v, approximately equaling 0.416. Furthermore, for the $M_t \approx 0.22$ cases, $\langle \Pi_l^{e_v} \rangle/(-\langle \mathcal{C}_{e_v}^\tau \rangle)$ is about 0.816 as $\langle K_\tau \rangle$ increases from 0.16 to 9.80, and reduces slightly from 0.833 to 0.732 with θ_v varying from 1.0 to 5.0. For the $M_t \approx 0.68$ cases, $\langle \Pi_l^{e_v} \rangle/(-\langle \mathcal{C}_{e_v}^\tau \rangle)$ is about 0.815.

Figures 14 and 15 show the PDFs of SGS fluxes for the translational–rotational and vibrational energy fluctuations based on the dilatational and solenoidal components of filtered velocity (i.e. $\Pi_l^{e_{tr},D}$, $\Pi_l^{e_{tr},S}$, $\Pi_l^{e_v,D}$ and $\Pi_l^{e_v,S}$) with $l/\eta \approx 15.37$. The PDFs of $\Pi_l^{e_{tr},D}$ and $\Pi_l^{e_v,D}$ are almost symmetrical about $\Pi_l^{e_{tr},D} = 0.0$ and $\Pi_l^{e_v,D} = 0.0$ (figures 14*a*,*c* and 15*a*,*c*). Obviously, the effect of vibrational relaxation on the fluctuations of $\Pi_l^{e_{tr},D}$ is much weaker than that of $\Pi_l^{e_v,D}$. The fluctuations of $\Pi_l^{e_v,D}$ decrease slightly

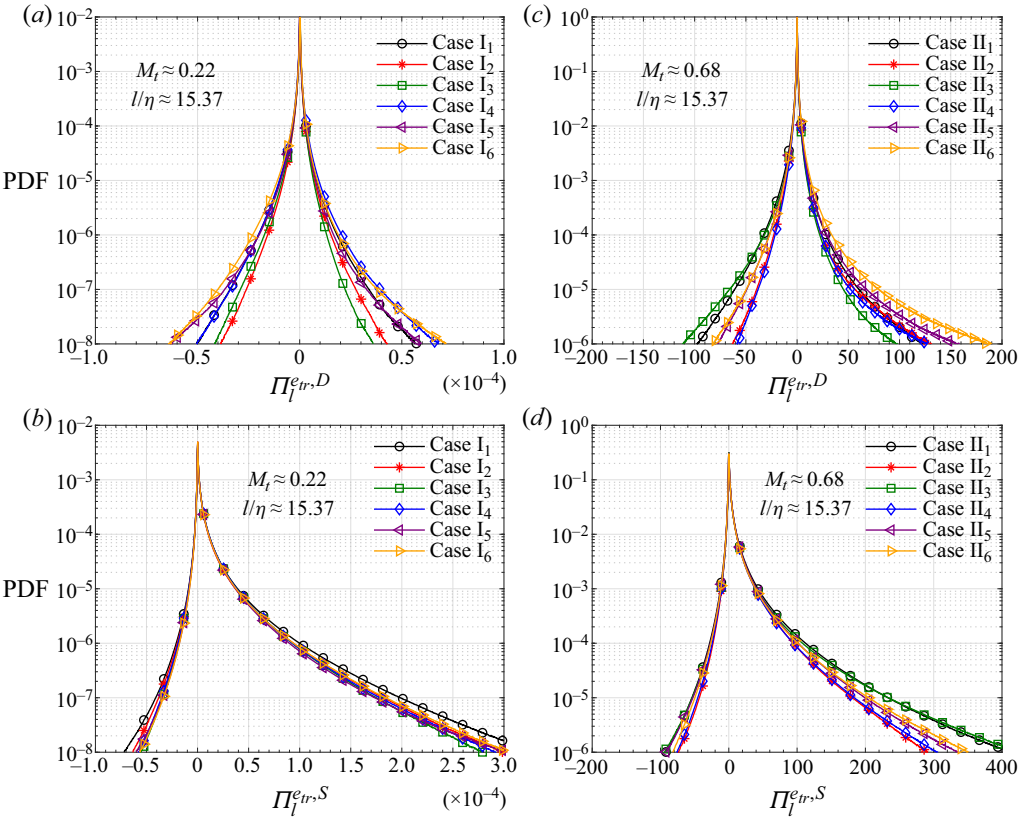

Figure 14. Probability density functions of SGS fluxes of translational–rotational energy fluctuation due to dilatational and solenoidal components of filtered velocity for $l/\eta \approx 15.37$. Here, (*a*,*b*) $M_t \approx 0.22$ and (*c*,*d*) $M_t \approx 0.68$.

with the increase of $\langle K_\tau \rangle$, and reduce significantly as θ_v increases. Meanwhile, the PDFs of $\Pi_l^{e_{tr},S}$ and $\Pi_l^{e_v,S}$ exhibit a significant skewness toward the positive side. As shown in figure 14(*b*,*d*), the PDFs of $\Pi_l^{e_{tr},S}$ of different cases roughly overlap each other. It means that the fluctuations of $\Pi_l^{e_{tr},S}$ are almost insensitive to the vibrational relaxation. The fluctuations of $\Pi_l^{e_v,S}$ are insensitive to $\langle K_\tau \rangle$ but are closely related to θ_v. With the increase of θ_v, the fluctuations of $\Pi_l^{e_v,S}$ diminish significantly (figure 15*b*,*d*). As shown in figure 14, the left tails of the PDFs of $\Pi_l^{e_{tr},D}$ and $\Pi_l^{e_{tr},S}$ are similar to each other, while the right tails of the PDFs of $\Pi_l^{e_{tr},S}$ are significantly longer than that of $\Pi_l^{e_{tr},D}$. This observation suggests that the contribution of dilatational velocity component to the direct SGS flux of translational–rotational energy fluctuation is much smaller than that of the solenoidal velocity component, while their contributions to the reverse SGS flux of translational–rotational energy fluctuation are similar. Consequently, the average SGS flux of translational–rotational energy fluctuation stems mainly from the solenoidal velocity component, which agrees well with the results in figure 13. Similar observations can be made in figure 15 for the SGS flux of vibrational energy fluctuation, from the PDFs of $\Pi_l^{e_v,D}$ and $\Pi_l^{e_v,S}$.

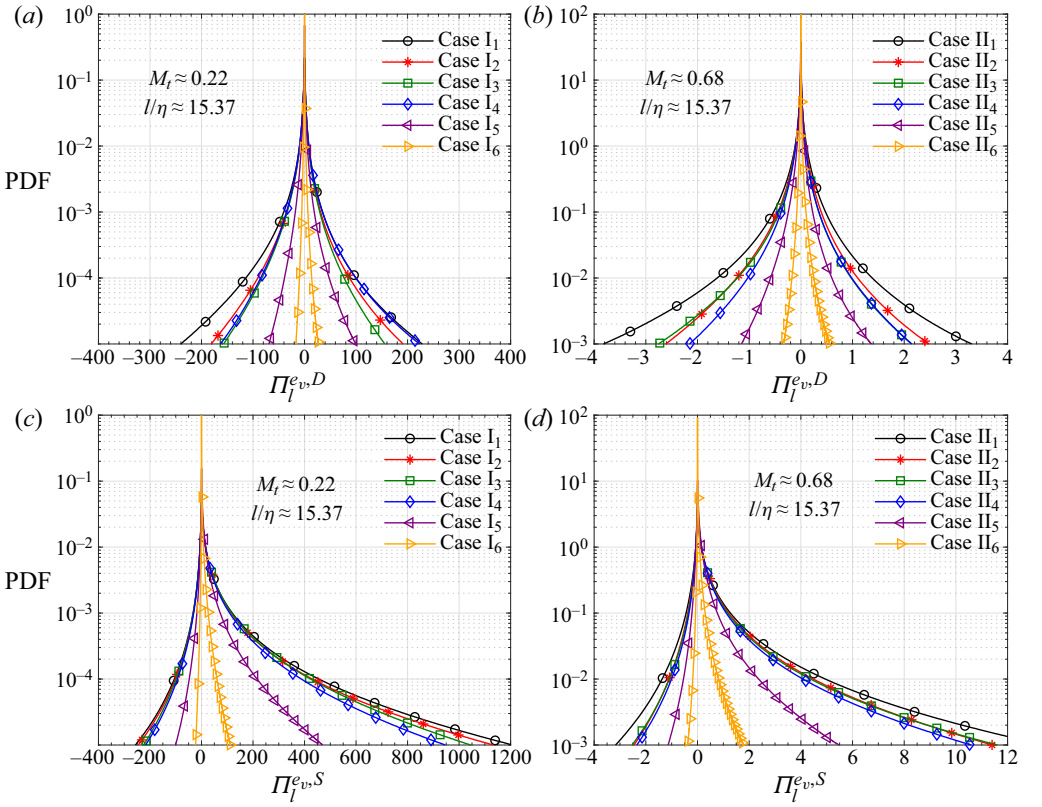

Figure 15. Probability density functions of SGS fluxes of vibrational energy fluctuation due to dilatational and solenoidal components of filtered velocity for $l/\eta \approx 15.37$. Here, (*a*,*b*) $M_t \approx 0.22$ and (*c*,*d*) $M_t \approx 0.68$.

To study the impact of local compressibility on the transfers of translational–rotational and vibrational energy fluctuations, the spatially averaged $(\Pi_l^{e_{tr},D} - \langle \Pi_l^{e_{tr},D} \rangle)$, $(\Pi_l^{e_{tr},S} - \langle \Pi_l^{e_{tr},S} \rangle)$, $(\Pi_l^{e_v,D} - \langle \Pi_l^{e_v,D} \rangle)$ and $(\Pi_l^{e_v,S} - \langle \Pi_l^{e_v,S} \rangle)$ conditioned on θ_l/θ_l' with $l/\eta \approx 15.37$ are presented in figures 16 and 17 for the $M_t \approx 0.22$ and 0.68 cases. Here, $\theta_l' = \sqrt{\langle \theta_l^2 \rangle}$ is the r.m.s. value of filtered velocity divergence. As shown in figures 16(*a*,*c*) and 17(*a*,*c*), $\langle \Pi_l^{e_{tr},D} - \langle \Pi_l^{e_{tr},D} \rangle | \theta_l/\theta_l' \rangle$ and $\langle \Pi_l^{e_v,D} - \langle \Pi_l^{e_v,D} \rangle | \theta_l/\theta_l' \rangle$ are positive in the compression region and negative in the expansion region, and their magnitudes enlarge with the increase of θ_l/θ_l' magnitude. Obviously, the vibrational relaxation has a great impact on the variation of $\langle \Pi_l^{e_{tr},D} - \langle \Pi_l^{e_{tr},D} \rangle | \theta_l/\theta_l' \rangle$ and $\langle \Pi_l^{e_v,D} - \langle \Pi_l^{e_v,D} \rangle | \theta_l/\theta_l' \rangle$. Taking the $M_t \approx 0.68$ cases as an example, with the increase of θ_v, the vibrational relaxation effect weakens, and $\langle \Pi_l^{e_{tr},D} - \langle \Pi_l^{e_{tr},D} \rangle | \theta_l/\theta_l' \rangle$ is greatly enhanced in the strong compression region (i.e. $\theta/\theta' \leq -2.0$), while $\langle \Pi_l^{e_v,D} - \langle \Pi_l^{e_v,D} \rangle | \theta_l/\theta_l' \rangle$ is significantly suppressed in the full flow field. As shown in figure 13, $\langle \Pi_l^{e_{tr},D} \rangle / \langle \mathcal{C}_{e_{tr}} \rangle \approx 0.0$ and $\langle \Pi_l^{e_v,D} \rangle / (-\langle \mathcal{C}_{e_v}^{\tau} \rangle) \approx 0.0$ with different l/η values. That is, the direct SGS fluxes of translational–rotational and vibrational energy fluctuations in the compression region are balanced by the reverse SGS fluxes in the expansion region. For the $M_t \approx 0.22$ cases, the variations of $\langle \Pi_l^{e_{tr},S} -$

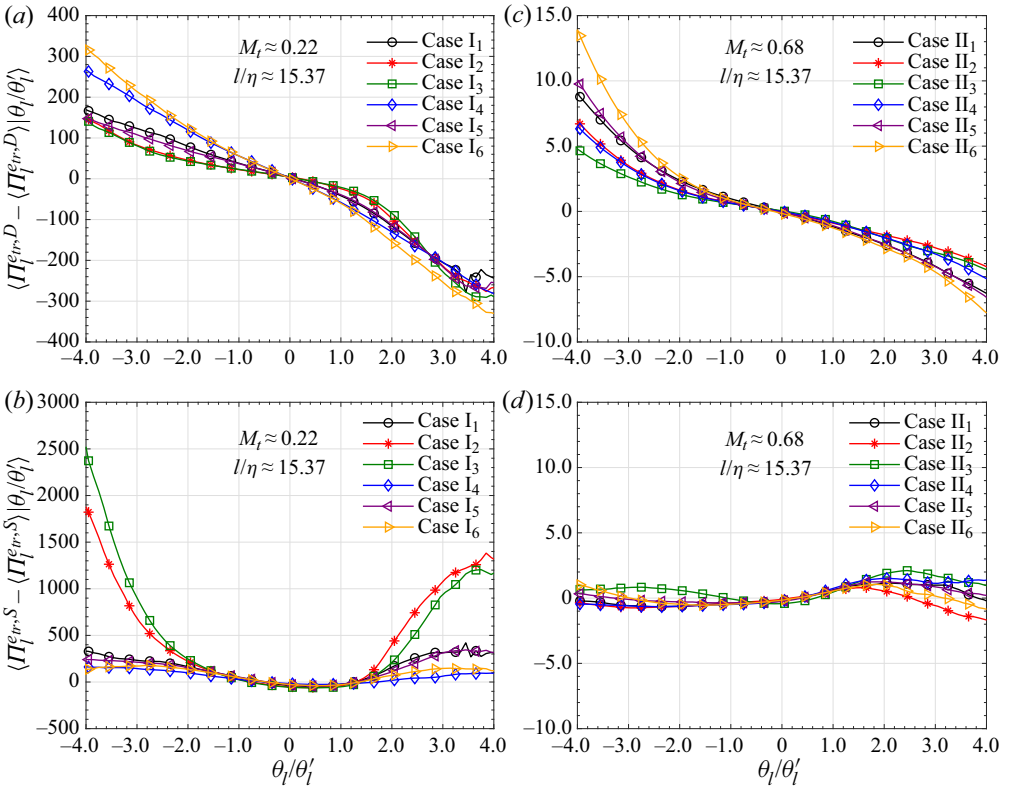

Figure 16. Spatial average of $(\Pi_l^{e_{tr},D} - \langle \Pi_l^{e_{tr},D} \rangle)$ and $(\Pi_l^{e_{tr},S} - \langle \Pi_l^{e_{tr},S} \rangle)$ conditioned on θ_l/θ_l'. Here, (*a*,*b*) $M_t \approx 0.22$ and (*c*,*d*) $M_t \approx 0.68$.

$\langle \Pi_l^{e_{tr},S} \rangle | \theta_l/\theta_l' \rangle$ and $\langle \Pi_l^{e_v,S} - \langle \Pi_l^{e_v,S} \rangle | \theta_l/\theta_l' \rangle$ are closely related to the vibrational relaxation (figures 16*b* and 17*b*). When the relaxation effect is significant, particularly for cases I_2 and II_3, both $\langle \Pi_l^{e_{tr},S} - \langle \Pi_l^{e_{tr},S} \rangle | \theta_l/\theta_l' \rangle$ and $\langle \Pi_l^{e_v,S} - \langle \Pi_l^{e_v,S} \rangle | \theta_l/\theta_l' \rangle$ approach 0.0 in the range of $|\theta_l/\theta_l'| \leq 1.6$, and increase sharply beyond this range. When the relaxation effect weakens, for instance, cases I_4 and I_6, $\langle \Pi_l^{e_{tr},S} - \langle \Pi_l^{e_{tr},S} \rangle | \theta_l/\theta_l' \rangle$ and $\langle \Pi_l^{e_v,S} - \langle \Pi_l^{e_v,S} \rangle | \theta_l/\theta_l' \rangle$ are almost insensitive to θ_l/θ_l'. Here, the sharp increase in the range of $|\theta_l/\theta_l'| \leq 1.6$ for cases I_2 and I_3 may result from the distinctive turbulent structure (fragmentized sheet-like structures) in the strong compression and expansion regions (figure 2).

For the $M_t \approx 0.68$ cases, $\langle \Pi_l^{e_{tr},S} - \langle \Pi_l^{e_{tr},S} \rangle | \theta_l/\theta_l' \rangle$ is about 0.0 (figure 16*d*). For these cases, the spatially averaged SGS fluxes of translational–rotational energy fluctuation due to the solenoidal velocity component are insensitive to the local compressibility in despite of the vibrational relaxation effect. However, $\langle \Pi_l^{e_v,S} - \langle \Pi_l^{e_v,S} \rangle | \theta_l/\theta_l' \rangle$ is negative in the compression region, and positive in the expansion region (figure 17*d*), although their dependence on the local compressibility is not as strong as that of $\langle \Pi_l^{e_v,D} - \langle \Pi_l^{e_v,D} \rangle | \theta_l/\theta_l' \rangle$. It suggests that the direct SGS flux of vibrational energy fluctuation due to the solenoidal velocity component weakens in the compression region, and enhances in the expansion region. The magnitude of $\langle \Pi_l^{e_v,S} - \langle \Pi_l^{e_v,S} \rangle | \theta_l/\theta_l' \rangle$ reduces as θ_v increases; for example, for case II_6, $\langle \Pi_l^{e_v,S} - \langle \Pi_l^{e_v,S} \rangle | \theta_l/\theta_l' \rangle$ approaches 0.0.

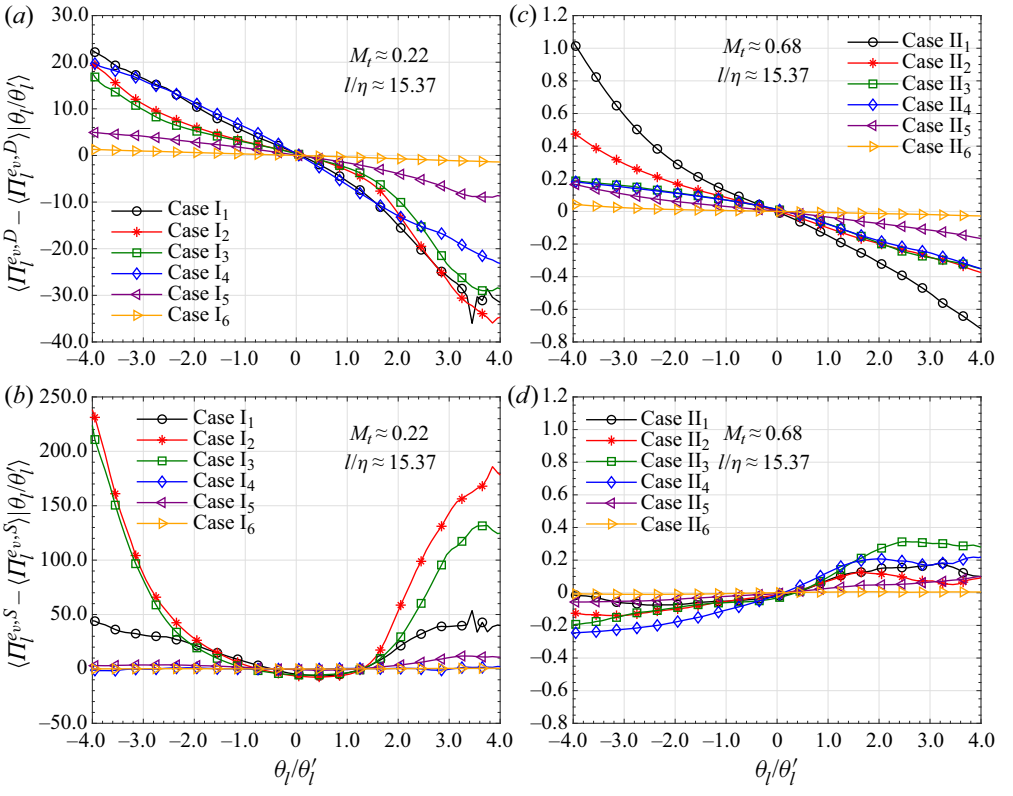

Figure 17. Spatial average of $(\Pi_l^{e_v,D} - \langle \Pi_l^{e_v,D} \rangle)$ and $(\Pi_l^{e_v,S} - \langle \Pi_l^{e_v,S} \rangle)$ conditioned on θ_l/θ_l'. Here, (a,b) $M_t \approx 0.22$ and (c,d) $M_t \approx 0.68$.

The geometrical variables for the SGS fluxes of translational–rotational and vibrational energy fluctuations are respectively defined as

$$\phi_l^{e_{tr}} = \boldsymbol{Q}^{e_{tr}} \cdot \boldsymbol{G}^{e_{tr}} / (|\boldsymbol{Q}^{e_{tr}}||\boldsymbol{G}^{e_{tr}}|) \tag{6.13}$$

and

$$\varphi_l^{e_v} = \boldsymbol{Q}^{e_v} \cdot \boldsymbol{G}^{e_v} / (|\boldsymbol{Q}^{e_v}||\boldsymbol{G}^{e_v}|), \tag{6.14}$$

where $Q_j^{e_{tr}} = \bar{\rho}(\widetilde{e_{tr_1} u_j} - \tilde{e}_{tr_1}\tilde{u}_j)$, $G_j^{e_{tr}} = (\partial/\partial x_j)(2\tilde{e}_{tr_1}/\bar{\rho})$ and $Q_j^{e_v} = \bar{\rho}(\widetilde{e_{v_1} u_j} - \tilde{e}_{v_1}\tilde{u}_j)$, $G_j^{e_v} = (\partial/\partial x_j)(2\tilde{e}_{v_1}/\bar{\rho})$.

Furthermore, the geometrical variables for SGS fluxes based on the solenoidal and dilatational components of filtered velocity can be defined as

$$\phi_l^{e_{tr},X} = \boldsymbol{Q}^{e_{tr},X} \cdot \boldsymbol{G}^{e_{tr}} / (|\boldsymbol{Q}^{e_{tr},X}||\boldsymbol{G}^{e_{tr}}|) \tag{6.15}$$

and

$$\varphi_l^{e_v,X} = \boldsymbol{Q}^{e_v,X} \cdot \boldsymbol{G}^{e_v} / (|\boldsymbol{Q}^{e_v,X}||\boldsymbol{G}^{e_v}|), \tag{6.16}$$

where $Q_j^{e_{tr},X} = \bar{\rho}(\widetilde{e_{tr_1} u_j^X} - \tilde{e}_{tr_1}\tilde{u}_j^X)$, $G_j^{e_{tr}} = (\partial/\partial x_j)(2\tilde{e}_{tr_1}/\bar{\rho})$ and $Q_j^{e_v,X} = \bar{\rho}(\widetilde{e_{v_1} u_j^X} - \tilde{e}_{v_1}\tilde{u}_j^X)$, $G_j^{e_v} = (\partial/\partial x_j)(2\tilde{e}_{v_1}/\bar{\rho})$. Here, X represents S or D.

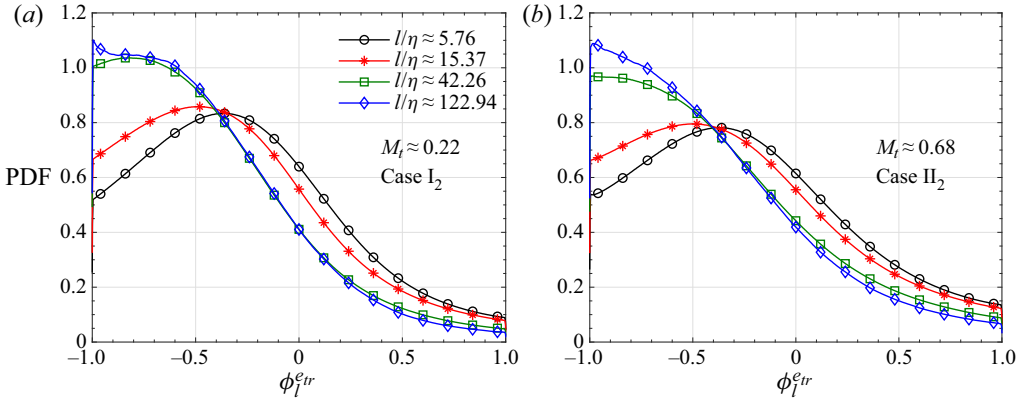

Figure 18. Probability density functions of geometrical variables for SGS fluxes of the translational–rotational energy fluctuation $\phi_l^{e_{tr}}$. (*a*) Case I_2, (*b*) case II_2.

Figure 18 presents the PDFs of $\phi_l^{e_{tr}}$ for cases I_2 and II_2 with different l/η values. It is found that the variations of PDFs with l/η are similar for cases I_2 and II_2. With $l/\eta \approx 122.94$ and 42.26, $\phi_l^{e_{tr}}$ has a tendency to be -1.0, which implies that the direct cascades of translational–rotational energy fluctuation are prominent in intermediate- and large-scale motions. With decreasing l/η (e.g. $l/\eta \approx 15.37$ and 5.76), peaks of the PDFs are approaching $\phi_l^{e_{tr}} = 0.0$, suggesting that in small-scale motions the direct cascades of translational–rotational energy fluctuation diminish. These observations are consistent with the results in figure 11, where $\langle \Pi_l^{e_{tr}} \rangle / \langle \mathcal{C}_{e_{tr}} \rangle$ increases gradually in $l/\eta \leq 20$, and remains roughly invariant in $20 \leq l/\eta \leq 80$.

The PDFs of $\phi_l^{e_{tr},D}$ and $\phi_l^{e_{tr},S}$ for the $M_t \approx 0.22$ and 0.68 cases with $l/\eta \approx 15.37$ are presented in figure 19. Interestingly, the PDFs of $\phi_l^{e_{tr},D}$ and $\phi_l^{e_{tr},S}$ with different $\langle K_\tau \rangle$ and θ_v values collapse. Furthermore, the PDFs of $\phi_l^{e_{tr},D}$ and $\phi_l^{e_{tr},S}$ for the $M_t \approx 0.22$ and 0.68 cases are close to each other. The PDFs of $\phi_l^{e_{tr},D}$ are approximately symmetrical about $\phi_l^{e_{tr},D} = 0.0$ (figure 19*a*,*c*), while the PDFs of $\phi_l^{e_{tr},S}$ almost overlap with those of $\phi_l^{e_{tr}}$ (figure 19*b*,*d*). The observation is consistent with the results in figure 13, i.e. the cascade of translational–rotational energy fluctuation is mainly dominated by the solenoidal component of filtered velocity. Furthermore, the effects of M_t and vibrational relaxation on the statistics of geometrical variables $\phi_l^{e_{tr},D}$ and $\phi_l^{e_{tr},S}$ are negligible. Note that the PDFs of $\varphi_l^{e_v}$ and $\varphi_l^{e_v,X}$ are extremely close to those of $\phi_l^{e_{tr}}$ and $\phi_l^{e_{tr},X}$ for both the $M_t \approx 0.22$ and 0.68 cases. For sake of simplicity, the PDFs of $\varphi_l^{e_v}$ and $\varphi_l^{e_v,X}$ are not presented.

7. Summary and conclusions

In this paper the statistically steady compressible isotropic turbulence in vibrational non-equilibrium is numerically investigated. Both the large-scale momentum forcing and thermal forcing are employed to maintain the turbulence in a statistically stationary state and to inject the large-scale temperature fluctuation. The turbulent Mach number (M_t) approximately equals 0.22 and 0.68, while the Taylor Reynolds number (Re_λ) is about 157.5. It is found that the large-scale thermal forcing enhances the flow compressibility,

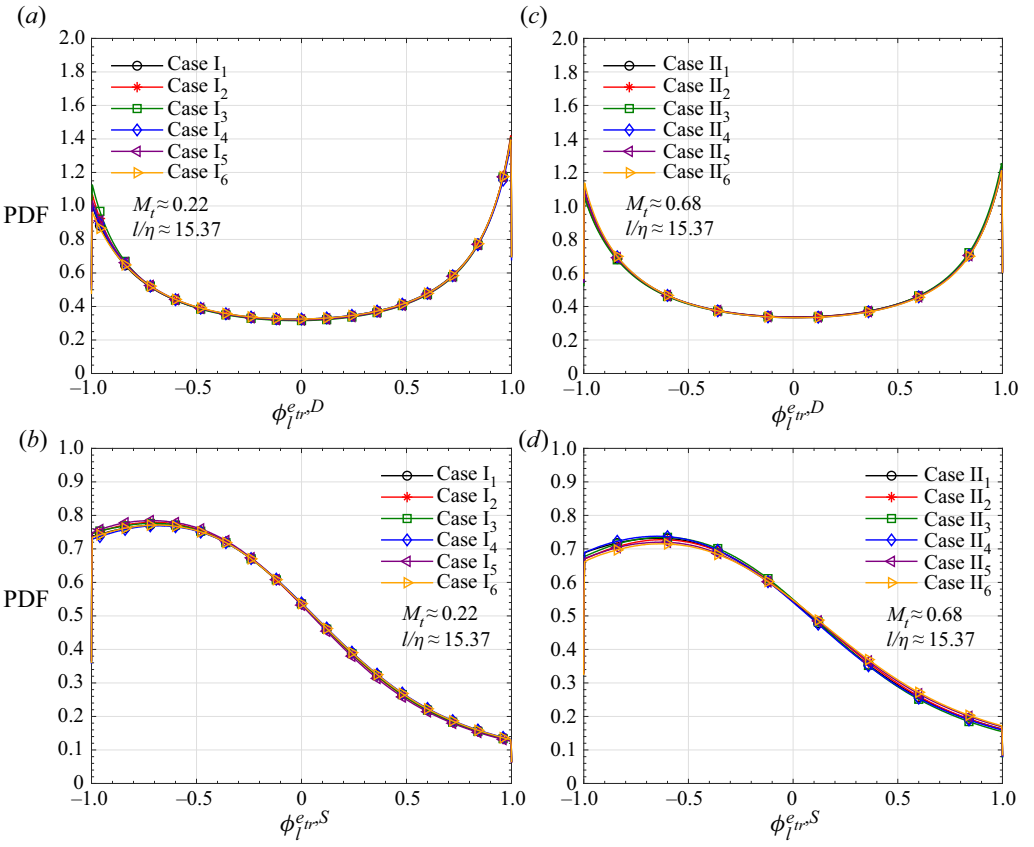

Figure 19. Probability density functions of geometrical variables for SGS fluxes of translational–rotational energy fluctuation. (*a*,*c*) Dilatational component $\phi_l^{e_{tr},D}$. (*b*,*d*) Solenoidal component $\phi_l^{e_{tr},S}$.

while the vibrational relaxation weakens it. The combined effects of large-scale thermal forcing and vibrational relaxation are significant in the $M_t \approx 0.22$ cases, and the effects diminish as M_t increases.

The velocity and pressure are decomposed into the solenoidal and dilatational components. The solenoidal velocity component is found to predominate over the dilatational component for both the $M_t \approx 0.22$ and 0.68 cases. The effects of M_t and vibrational relaxation on the fluctuations of solenoidal velocity and pressure components are insignificant. However, the fluctuations of their dilatational components are closely related on the M_t and vibrational relaxation. For both the $M_t \approx 0.22$ and 0.68 cases, the spectra of velocity, solenoidal pressure component, density and temperatures exhibit a $k^{-5/3}$ scaling at intermediate wavenumbers. The present $k^{-5/3}$ scaling for the spectrum of solenoidal pressure component should be attributed to the finite-Reynolds-number effect. For the $M_t \approx 0.22$ cases, because of the large-scale thermal forcing, the fluctuations of pressure and its dilatational component at low wavenumbers are much larger than their counterparts for the $M_t \approx 0.68$ cases. When the relaxation effect is significant, the fluctuation of pressure is mainly dominated by the dilatational component at low wavenumbers, and by the solenoidal component at intermediate and high wavenumbers. When the relaxation effect weakens, the fluctuation of pressure at full wavenumbers is largely dominated by the dilatational component. For the $M_t \approx 0.68$ cases, the large-scale

thermal forcing does not increase the fluctuations of pressure and its dilatational component at low wavenumbers. The spectra of pressure and its dilatational component exhibit approximately the $k^{-5/3}$ scaling at the intermediate wavenumbers. The fluctuation of dilatational pressure component is comparable to that of the solenoidal component at low and intermediate wavenumbers, while the pressure fluctuation is dominated by the dilatational component at high wavenumbers.

The weak form of acoustic equilibrium hypothesis is validated for both the $M_t \approx 0.22$ and 0.68 cases, i.e. $\chi = \langle p\rangle\gamma_r M_t(u^D_{rms}/u')/p^D_{rms} \approx 1.0$. However, for the $M_t \approx 0.22$ cases, the strong acoustic equilibrium hypothesis ($E^{p^D}(k) = 2.0\gamma_r\langle\rho\rangle\langle p\rangle E^{u^D}(k)$) is valid only at low wavenumbers when the vibrational relaxation effect is significant, and it is approximately valid at all wavenumbers as the vibrational relaxation effect weakens. For the $M_t \approx 0.68$ cases, the strong acoustic equilibrium hypothesis is valid at all wavenumbers in despite of the vibrational relaxation.

On global average, the change rates of translational–rotational energy fluctuation due to the dilatation and viscosity are negligible for both the $M_t \approx 0.22$ and 0.68 cases. The dissipation rate of translational–rotational energy fluctuation stems mainly from the thermal conduction and vibrational relaxation, while the former plays a major role. For both the $M_t \approx 0.22$ and 0.68 cases, the change rate of vibrational energy fluctuation due to the dilatation effect is negligible, while the dissipation rate of vibrational energy fluctuation due to the thermal conduction is comparable to the production rate owing to the vibrational relaxation.

The Favre filtering approach is adopted to investigate the transfers of translational–rotational and vibrational energy fluctuations. The SGS flux terms are further decomposed into the solenoidal and dilatational components. For both the $M_t \approx 0.22$ and 0.68 cases, the cascades of translational–rotational and vibrational energy fluctuations exist in the range of $20 \leq l/\eta \leq 80$. The spatially averaged SGS fluxes of translational–rotational and vibrational energy fluctuations are mainly dominated by the solenoidal component of filtered velocity. The spatially averaged SGS fluxes due to the dilatational component of filtered velocity depends closely on the local compressibility, M_t and vibrational relaxation. The direct SGS fluxes in the compression region is balanced by the reverse SGS fluxes in the expansion region. Furthermore, for the $M_t \approx 0.22$ cases, the spatially averaged SGS fluxes of translational–rotational and vibrational energy fluctuations based on the solenoidal component of filtered velocity increase sharply with the compressibility in the strong compression and expansion regions. The sensibility to the local compressibility gradually disappears as the relaxation effect weakens. However, for the $M_t \approx 0.68$ cases, the spatially averaged SGS flux of translational–rotational energy fluctuation due to the solenoidal component of filtered velocity is almost insensitive to the local compressibility, while that of the vibrational energy fluctuation has a weak connection with the local compressibility.

Funding. This work is supported by the NSFC Basic Science Center Program for Multiscale Problems in Nonlinear Mechanics (grant no. 11988102), National Natural Science Foundation of China (grant nos. 11702127, 91752201, 91952104 and 11902139), China Postdoctoral Science Foundation (grant no. 2019M652703), Technology and Innovation Commission of Shenzhen Municipality (grant nos. KQTD20180411143441009 and JCYJ20170412151759222), and by Department of Science and Technology of Guangdong Province (grant no. 2019B21203001). This work is also supported by Center for Computational Science and Engineering of Southern University of Science and Technology. J.W. acknowledges the support from Young Elite Scientist Sponsorship Program by CAST (grant no. 2016QNRC001).

Declaration of interests. The authors report no conflict of interest.

Author ORCIDs.
Qinmin Zheng https://orcid.org/0000-0002-0188-4835;
Jianchun Wang https://orcid.org/0000-0001-5101-7791;
Md. Mahbub Alam https://orcid.org/0000-0001-7937-8556;
Bernd R. Noack https://orcid.org/0000-0001-5935-1962.

Appendix A. Forcing strategy

In present simulations, the large-scale momentum forcing is only applied to the solenoidal component of the velocity field. Such a forcing strategy is wildly employed in homogeneous isotropic turbulence (Donzis & John 2020). The velocity field $\boldsymbol{u}(\boldsymbol{x}, t)$ is transformed into the Fourier space to yield $\hat{\boldsymbol{u}}(\boldsymbol{k}, t)$, which is further decomposed into a solenoidal field ($\hat{\boldsymbol{u}}^S(\boldsymbol{k}, t)$) and a dilatational field ($\hat{\boldsymbol{u}}^D(\boldsymbol{k}, t)$). Here, $\boldsymbol{k}$ is a wave vector in Fourier space. Similarly, the kinetic energy per unit mass for each wave vector can be decomposed as

$$\frac{|\hat{\boldsymbol{u}}(\boldsymbol{k}, t)|^2}{2} = \frac{|\hat{\boldsymbol{u}}^S(\boldsymbol{k}, t)|^2}{2} + \frac{|\hat{\boldsymbol{u}}^D(\boldsymbol{k}, t)|^2}{2}. \tag{A1}$$

The kinetic energy in each of the first two wavenumber shells can be calculated as

$$E^u(0.5 \le k < 1.5) = \sum_{0.5 \le |\boldsymbol{k}| < 1.5} \left(\frac{|\hat{\boldsymbol{u}}(\boldsymbol{k}, t)|^2}{2} \right) \tag{A2}$$

$$\text{and} \quad E^u(1.5 \le k < 2.5) = \sum_{1.5 \le |\boldsymbol{k}| < 2.5} \left(\frac{|\hat{\boldsymbol{u}}(\boldsymbol{k}, t)|^2}{2} \right). \tag{A3}$$

Similarly, the kinetic energy in the first two wavenumber shells can be decomposed as

$$E^u(0.5 \le k < 1.5) = E^{u,S}(0.5 \le k < 1.5) + E^{u,D}(0.5 \le k < 1.5), \tag{A4}$$

$$\text{and} \quad E^u(1.5 \le k < 2.5) = E^{u,S}(1.5 \le k < 2.5) + E^{u,D}(1.5 \le k < 2.5). \tag{A5}$$

To maintain the total kinetic energy in the first two shells to the prescribed levels $E_u(1)$ and $E_u(2)$, respectively, the solenoidal velocity field ($\hat{\boldsymbol{u}}^S(\boldsymbol{k}, t)$) is amplified, while the dilatational velocity field ($\hat{\boldsymbol{u}}^D(\boldsymbol{k}, t)$) is left untouched. The forced velocity field $\hat{\boldsymbol{u}}^f(\boldsymbol{k}, t)$ is given as

$$\hat{\boldsymbol{u}}^f(\boldsymbol{k}, t) = \alpha \hat{\boldsymbol{u}}^S(\boldsymbol{k}, t) + \hat{\boldsymbol{u}}^D(\boldsymbol{k}, t), \tag{A6}$$

where α for all modes in each wavenumber shell is set to be

$$\alpha(0.5 \le k < 1.5) = \sqrt{\frac{E^u(1) - E^{u,D}(0.5 \le k < 1.5)}{E^{u,S}(0.5 \le k < 1.5)}} \tag{A7}$$

$$\text{and} \quad \alpha(1.5 \le k < 2.5) = \sqrt{\frac{E^u(2) - E^{u,D}(1.5 \le k < 2.5)}{E^{u,S}(1.5 \le k < 2.5)}}. \tag{A8}$$

Here, $E^u(1) = 1.242477$ and $E^u(2) = 0.391356$.

The large-scale thermal forcing for the translational–rotational temperature (T_{tr}) field is similar to that for the solenoidal velocity field. The translational–rotational temperature

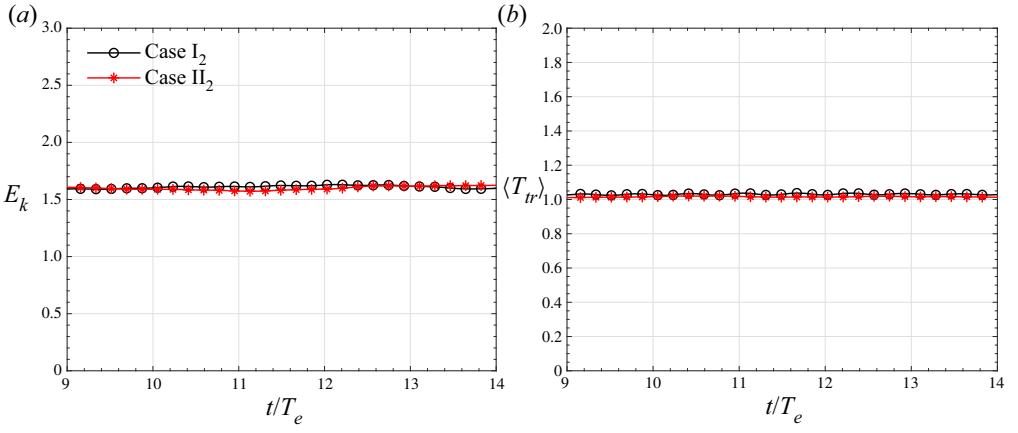

Figure 20. Time evolution of spatially averaged (*a*) kinetic energy ($E_k = \langle \boldsymbol{u}^2 \rangle/2$) and (*b*) translational–rotational temperature ($\langle T_{tr} \rangle$).

field $T_{tr}(\boldsymbol{x}, t)$ is transformed into the Fourier space to yield $\hat{T}_{tr}(\boldsymbol{k}, t)$. Similarly,

$$E^{T_{tr}}(0.5 \leq k < 1.5) = \sum_{0.5 \leq |\boldsymbol{k}| < 1.5} (|\hat{T}_{tr}(\boldsymbol{k}, t)|^2) \tag{A9}$$

$$\text{and} \quad E^{T_{tr}}(1.5 \leq k < 2.5) = \sum_{1.5 \leq |\boldsymbol{k}| < 2.5} (|\hat{T}_{tr}(\boldsymbol{k}, t)|^2). \tag{A10}$$

The forced translational–rotational temperature is given as

$$\hat{T}^f_{tr}(\boldsymbol{k}, t) = \beta \hat{T}_{tr}(\boldsymbol{k}, t), \tag{A11}$$

where β for all modes in each wavenumber shell is set to be

$$\beta(0.5 \leq k < 1.5) = \sqrt{\frac{E^{T_{tr}}(1)}{E^{T_{tr}}(0.5 \leq k < 1.5)}} \tag{A12}$$

$$\text{and} \quad \beta(1.5 \leq k < 2.5) = \sqrt{\frac{E^{T_{tr}}(2)}{E^{T_{tr}}(1.5 \leq k < 2.5)}}. \tag{A13}$$

Here, $E^{T_{tr}}(1) = E^u(1)/100$ and $E^{T_{tr}}(2) = E^u(2)/100$.

Figure 20 shows the time evolution of spatially averaged kinetic energy ($E_k = \langle \boldsymbol{u}^2 \rangle/2$) and translational–rotational temperature ($\langle T_{tr} \rangle$) in the sampling period for cases I_2 and II_2. The values of $E_k = \langle \boldsymbol{u}^2 \rangle/2$ and $\langle T_{tr} \rangle$ keep almost constant with a slight fluctuation. The $E_k \approx 1.61$ and $\langle T_{tr} \rangle \approx 1.03$. It reveals that the present simulated flows are in a statistically stationary state in the sampling period.

References

Alexakis, A. & Biferale, L. 2018 Cascades and transitions in turbulent flows. *Phys. Rep.* **767**, 1–101.

Aluie, H. 2011 Compressible turbulence: the cascade and its locality. *Phys. Rev. Lett.* **106** (17), 174502.

Aluie, H. 2013 Scale decomposition in compressible turbulence. *Physica* D **247** (1), 54–65.

Aluie, H., Li, S. & Li, H. 2012 Conservative cascade of kinetic energy in compressible turbulence. *Astrophys. J. Lett.* **751** (2), L29.

ANDERSON, J.D. JR. 2006 *Hypersonic and High-Temperature Gas Dynamics*. American Institute of Aeronautics and Astronautics.
BALSARA, D.S. & SHU, C.-W. 2000 Monotonicity preserving weighted essentially non-oscillatory schemes with increasingly high order of accuracy. *J. Comput. Phys.* **160** (2), 405–452.
BERTOLOTTI, F.P. 1998 The influence of rotational and vibrational energy relaxation on boundary-layer stability. *J. Fluid Mech.* **372**, 93–118.
BOSE, T.K. 2014 High temperature gas dynamics. In *High Temperature Gas Dynamics*. Springer.
CANDLER, G.V. 2019 Rate effects in hypersonic flows. *Annu. Rev. Fluid Mech.* **51** (1), 379–402.
CARDY, J., FALKOVICH, G. & GAWEDZKI, K. 2008 *Nonequilibrium Statistical Mechanics and Turbulence*, vol. 355. Cambridge University Press.
COLONNA, G., BONELLI, F. & PASCAZIO, G. 2019 Impact of fundamental molecular kinetics on macroscopic properties of high-enthalpy flows: the case of hypersonic atmospheric entry. *Phys. Rev. Fluids* **4** (3), 033404.
DOBLER, W., HAUGEN, N.E.L., YOUSEF, T.A. & BRANDENBURG, A. 2003 Bottleneck effect in three-dimensional turbulence simulations. *Phys. Rev.* E **68** (2), 026304.
DONZIS, D. & JAGANNATHAN, S. 2013 Fluctuations of thermodynamic variables in stationary compressible turbulence. *J. Fluid Mech.* **733**, 221–244.
DONZIS, D.A. 2012 Shock structure in shock-turbulence interactions. *Phys. Fluids* **24** (12), 126101.
DONZIS, D.A. & JOHN, J.P. 2020 Universality and scaling in homogeneous compressible turbulence. *Phys. Rev. Fluids* **5** (8), 084609.
DONZIS, D.A. & MAQUI, A.F. 2016 Statistically steady states of forced isotropic turbulence in thermal equilibrium and non-equilibrium. *J. Fluid Mech.* **797**, 181–200.
DONZIS, D.A. & SREENIVASAN, K.R. 2010 The bottleneck effect and the kolmogorov constant in isotropic turbulence. *J. Fluid Mech.* **657**, 171–188.
EYINK, G.L. & DRIVAS, T.D. 2018 Cascades and dissipative anomalies in compressible fluid turbulence. *Phys. Rev.* X **8** (1), 011022.
FIÉVET, R. & RAMAN, V. 2018 Effect of vibrational nonequilibrium on isolator shock structure. *J. Propul. Power* **34** (5), 1334–1344.
FRISCH, U. 1995 *Turbulence: The Legacy of A. N. Kolmogorov*. Cambridge University Press.
GOTOH, T. & FUKAYAMA, D. 2001 Pressure spectrum in homogeneous turbulence. *Phys. Rev. Lett.* **86** (17), 3775–3778.
GOTOH, T. & ROGALLO, R.S. 1999 Intermittency and scaling of pressure at small scales in forced isotropic turbulence. *J. Fluid Mech.* **396**, 257–285.
GOTTLIEB, S. & SHU, C.-W. 1998 Total variation diminishing Runge–Kutta schemes. *Maths Comput.* **67** (221), 73–85.
HIRSCHFELDER, J.O., CURTISS, C.F., BIRD, R.B. & MAYER, M.G. 1964 *Molecular Theory of Gases and Liquids*, vol. 165. Wiley.
JAGANNATHAN, S. & DONZIS, D. 2016 Reynolds and mach number scaling in solenoidally-forced compressible turbulence using high-resolution direct numerical simulations. *J. Fluid Mech.* **789**, 669–707.
JOSYULA, E. 2015 *Hypersonic Nonequilibrium Flows: Fundamentals and Recent Advances*. American Institute of Aeronautics and Astronautics.
KHURSHID, S. & DONZIS, D.A. 2019 Decaying compressible turbulence with thermal non-equilibrium. *Phys. Fluids* **31** (1), 015103.
KNISELY, C.P. & ZHONG, X. 2020 Impact of vibrational nonequilibrium on the supersonic mode in hypersonic boundary layers. *AIAA J.* **58** (4), 1704–1714.
KOLMOGOROV, A.N. 1991 The local structure of turbulence in incompressible viscous fluid for very large Reynolds numbers. *Proc. R. Soc. Lond.* A **434** (1890), 9–13.
LELE, S.K. 1992 Compact finite difference schemes with spectral-like resolution. *J. Comput. Phys.* **103** (1), 16–42.
LI, D., ZHANG, X. & HE, G. 2013 Temporal decorrelations in compressible isotropic turbulence. *Phys. Rev.* E **88** (2), 021001.
LIAO, W., PENG, Y. & LUO, L.-S. 2010 Effects of multitemperature nonequilibrium on compressible homogeneous turbulence. *Phys. Rev.* E **81** (4), 046704.
MARTIN, M.P., PIOMELLI, U. & CANDLER, G.V. 2000 Subgrid-scale models for compressible large-eddy simulations. *Theor. Comput. Fluid Dyn.* **13** (5), 361–376.
MELDI, M. & SAGAUT, P. 2013 Pressure statistics in self-similar freely decaying isotropic turbulence. *J. Fluid Mech.* **717**, R2.
NI, Q. 2015 Compressible turbulent mixing: effects of schmidt number. *Phys. Rev.* E **91**, 053020.

NOMPELIS, I., CANDLER, G.V. & HOLDEN, M.S. 2003 Effect of vibrational nonequilibrium on hypersonic double-cone experiments. *AIAA J.* **41** (11), 2162–2169.

PAN, S. & JOHNSEN, E. 2017 The role of bulk viscosity on the decay of compressible, homogeneous, isotropic turbulence. *J. Fluid Mech.* **833**, 717–744.

PASSOT, T., VÁZQUEZ-SEMADENI, E. & POUQUET, A. 1995 A turbulent model for the interstellar medium. II. Magnetic fields and rotation. *Astrophys. J.* **455**, 536–555.

RICH, J.W. & TREANOR, C.E. 1970 Vibrational relaxation in gas-dynamic flows. *Annu. Rev. Fluid Mech.* **2** (1), 355–396.

SAGAUT, P. & CAMBON, C. 2008 *Homogeneous Turbulence Dynamics*. Springer.

SAMTANEY, R., PULLIN, D.I. & KOSOVIĆ, B. 2001 Direct numerical simulation of decaying compressible turbulence and shocklet statistics. *Phys. Fluids* **13** (5), 1415–1430.

SCHMIDT, W. & GRETE, P. 2019 Kinetic and internal energy transfer in implicit large-eddy simulations of forced compressible turbulence. *Phys. Rev.* E **100** (4), 043116.

SCIACOVELLI, L., CINNELLA, P. & GRASSO, F. 2017 Small-scale dynamics of dense gas compressible homogeneous isotropic turbulence. *J. Fluid Mech.* **825**, 515–549.

SHI, L., SHEN, H., ZHANG, P., ZHANG, D. & WEN, C. 2017 Assessment of vibrational non-equilibrium effect on detonation cell size. *Combust. Sci. Technol.* **189** (5), 841–853.

TSUJI, Y. & ISHIHARA, T. 2003 Similarity scaling of pressure fluctuation in turbulence. *Phys. Rev.* E **68** (2), 026309.

URZAY, J. 2018 Supersonic combustion in air-breathing propulsion systems for hypersonic flight. *Annu. Rev. Fluid Mech.* **50**, 593–627.

VEDULA, P. & YEUNG, P.K. 1999 Similarity scaling of acceleration and pressure statistics in numerical simulations of isotropic turbulence. *Phys. Fluids* **11** (5), 1208–1220.

VINCENTI, W.G. & KRUGER, C.H. 1965 *Introduction to Physical Gas Dynamics*. Wiley.

WANG, J., GOTOH, T. & WATANABE, T. 2017 Spectra and statistics in compressible isotropic turbulence. *Phys. Rev. Fluids* **2** (1), 013403.

WANG, J., SHI, Y., WANG, L.-P., XIAO, Z., HE, X. & CHEN, S. 2011 Effect of shocklets on the velocity gradients in highly compressible isotropic turbulence. *Phys. Fluids* **23** (12), 125103.

WANG, J., WAN, M., CHEN, S. & CHEN, S. 2018 Kinetic energy transfer in compressible isotropic turbulence. *J. Fluid Mech.* **841**, 581–613.

WANG, J., WAN, M., CHEN, S., XIE, C., WANG, L.-P. & CHEN, S. 2019 Cascades of temperature and entropy fluctuations in compressible turbulence. *J. Fluid Mech.* **867**, 195–215.

WANG, J., WANG, L.-P., XIAO, Z., SHI, Y. & CHEN, S. 2010 A hybrid numerical simulation of isotropic compressible turbulence. *J. Comput. Phys.* **229** (13), 5257–5279.

ZHENG, Q., WANG, J., NOACK, B.R., LI, H., WAN, M. & CHEN, S. 2020 Vibrational relaxation in compressible isotropic turbulence with thermal nonequilibrium. *Phys. Rev. Fluids* **5**, 044602.